

Coarse-graining active tension nets with discrete conformal geometry

Nikolas H. Claussen*

Princeton Center for Theoretical Science, Princeton University, Princeton, New Jersey 08542, USA

Fridtjof Brauns†

Max Planck Institute for the Physics of Complex Systems, Nöthnitzer Straße 38, 01187 Dresden, Germany

Max Planck Institute of Molecular Cell Biology and Genetics,

Pfotenhauerstraße 108, 01307 Dresden, Germany and

Center for Systems Biology Dresden, 01307 Dresden, Germany

Boris I. Shraiman‡

Kavli Institute for Theoretical Physics, University of California, Santa Barbara, California 93106, USA

In contrast to inert materials, living cells use molecular motors to generate forces independently of elastic strain. How do local active forces translate into large-scale shape, and what are the mechanical properties of the resulting “living matter”? Here, we address these questions within the active tension network (ATN) model for the mechanics of 2d epithelia. We represent the configuration of active forces geometrically by a tension triangulation dual to the cell tessellation. The Voronoi dual of the tension triangulation is shown to be macroscopically stress-free – the tensions hence define an emergent reference state for the tissue. Two soft modes, curl-free and conformal deformations, map this reference to the internally stressed, but force-balanced, physical configuration of the tissue. Conformal deformations parametrize pressure gradients, leading to a generalization of von Neumann’s law for the pressure in a foam. Via finite-element-like interpolation and a notion of “discrete” conformal maps, we both construct the mechanically balanced cell tessellations exactly on the microscopic level, and pass to the continuum limit. We systematically incorporate cell rearrangement into our theory by representing cell-scale topology in terms of circle packings. The results of this bottom-up coarse-graining study match a top-down continuum analysis presented in a companion paper. Thus, the geometry of force balance bridges between micro- and macro-scales, elucidating how cell-level active forces program shape. The present formalism may be useful in the study of foams, granular matter, and metamaterials, as well as in numerical simulations.

INTRODUCTION

Active materials are characterized by their ability to locally generate active forces, independent of elastic or viscoelastic stresses [1]. Living tissues are a paradigmatic example, generating active stress via motor molecules in the cytoskeleton [2]. Notably, during morphogenesis, cells use these “microscopic muscles” to sculpt the form of the embryonic body [3]. Understanding the large-scale consequences of cell-scale active forces, and how active tissue reacts to external forces (e.g., fluid- or solid-like), is an important question in biological physics. More precisely, we aim to understand, first, how local active forces determine the large-scale shape of a tissue – the mechanical ground state –, and second, how this shape reacts to additional forces – the low-energy excitations.

Put another way, there is a crucial distinction between the microscopic and macroscopic stress state of a tissue. A raft of soap bubbles illustrates this point: individual bubble interfaces are under (surface) tension, while the raft as a whole is stable even if its boundaries are free. The raft is hence macroscopically stress-free. Biologi-

cally, tensions and macroscopic stress can be assessed by different laser ablation experiments: severing single cell interfaces, or cutting out a patch comprising a mesoscopic number of cells (Fig. 1). Currently, a systematic framework to connect these scales is missing. One reason for this is the complexity of many cell-resolved models.

In many cell-level (and continuum) models for tissue mechanics, active forces are modeled as an additional “drive” on top of a visco-elastic “backbone” [4, 5]. Dynamics are set by frictional or viscous relaxation. Such models can become quite complex [4], making it hard to understand the physical consequences of active forces. To simplify, we make use of a separation of biological timescales. Due to the rapidity of mechanical relaxation (10s of seconds [6]), tissues are typically in adiabatic force balance [7]. Furthermore, because molecular turnover [2] leads to viscous relaxation of passive, elastic stresses, one expects that on long timescales, active, motor-molecule-generated stresses dominate.

Here, we study the mechanics of active tension networks (ATN) [8, 9], a minimal model for 2d epithelia, dominated by active interfacial tensions. Intuitively, the ATN model describes a tissue as a generalized, active foam [10]. In contrast to a conventional fluid foam, where the fluid’s surface tension is a fixed material parameter, cells actively regulate their interfacial tensions. By casting the mechanics of ATNs in geometric terms, we will

* nc1333@princeton.edu

† fbrauns@pks.mpg.de

‡ shraiman@ucsb.edu

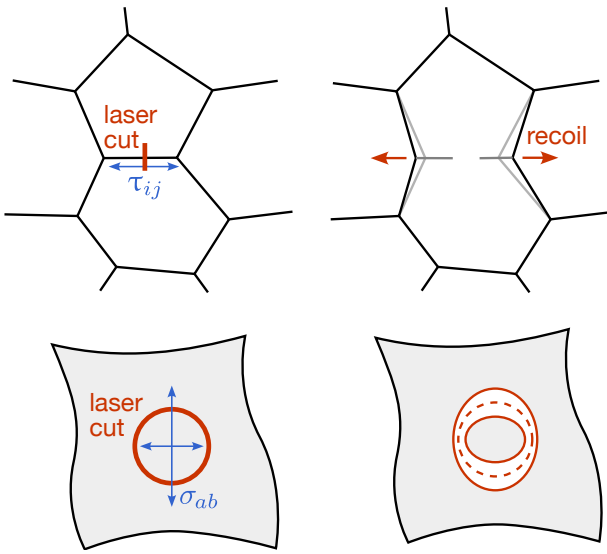


FIG. 1. Top: Laser ablations of individual junctions measure the tension τ_{ij} on an individual cell-cell interface (i, j label adjacent cells). Bottom: Laser ablations on the tissue scale measure the macroscopic stress tensor σ_{ab} (where a, b are coordinate indices).

determine the mechanical “phase of matter” of the tissue. We show how local contractile activity determines the large-scale shape and stress of the tissue and identify the soft modes that govern the response to external forces. Overall, we find that ATNs exhibit *emergent elasticity*: a macroscopically stress-free reference state and an effective stress-strain relationship emerge from the configurations of active tensions.

This work presents a coarse-graining analysis, starting from the “microscopic” ATN model. In a companion paper, Ref. [11], we derive and analyze the effective long-wavelength theory directly in the continuum.

Background and motivation

Active tension networks in 2D

We first review the cell-based ATN model [8, 9]. We consider a 2d epithelial tissue whose cells i, j, \dots form a confluent tessellation (a, b, \dots denote spatial indices), and whose mechanics is dominated by interfacial tensions τ_{ij} and intracellular pressure p_i . The tri-cellular vertices of the cell tessellation are written \mathbf{r}_{ijk} . ATNs are thus a type of “vertex model” [4]: they represent the tissue by a polygonal tiling with vertices \mathbf{r}_{ijk} . However, as we will see below, the effective degrees of freedom are geometric “collective modes” coupling multiple vertices.

The configuration of the tissue is determined by me-

chanical balance – virtual work has to vanish

$$0 = dE = - \sum_{i \sim j} \tau_{ij} d\ell_{ij} + \sum_i p_i a_i \quad (1)$$

where ℓ_{ij} and a_i are interface lengths and cell areas and (ij) denotes all adjacent cell pairs. A constitutive relation (cell bulk elasticity) determines the pressures p_i :

$$p_i = P(a_i) \quad (2)$$

By contrast, the interfacial tensions τ_{ij} are dynamical variables independent of interfacial lengths ℓ_{ij} , and instead determined by the local activity of motor molecules.

Therefore, the energy of an edge is *linear* in ℓ_{ij} , rather than quadratic, as it would be for a Hookean spring. This feature is shared with fluid films [12] in a foam. Eq. (1) is thus the elastic energy of a *generalized foam*: in an ordinary fluid foam, all interfacial tensions are equal $\tau_{ij} = \tau$, determined by the fluid’s surface tension. In a generalized foam, the tensions are upgraded to independent, dynamical variables.

While the ATN model shares the physical DOFs (vertex positions) of the much-studied area-perimeter vertex model [13, 14], it fundamentally differs in the microscopic mechanics. The area-perimeter vertex model assumes a particular physical reference configuration and constitutive law, encoded in the elastic energy $E_{AP} = \sum_i k_A(a_0 - a_i)^2 + k_p(P_0 - \sum_{j \sim i} \ell_{ij})^2$. Here, a_0, P_0 are a cell’s target area and perimeter, k_A, k_p are generalized spring constants, and $j \sim i$ denotes all neighbors of cell i . The area-perimeter vertex model, therefore, describes a particular kind of spring network.

As we argue in the following, in ATNs, an *effective* reference configuration and constitutive law emerge at large scales, even though microscopically, active tensions (stress) and edge lengths (strain) are independent.

Continuum mechanics of ATNs

In the companion paper [11], we derived a continuum theory that describes the behavior of the ATN model at large, supracellular length scales. The key to this approach is to think of the tension configuration as a *triangulation* with nodes i, j, \dots and edge lengths τ_{ij} . In the continuum limit, a set of arbitrary, Lagrangian coordinates ξ plays the role of the cell labels i, j, \dots . The discrete tension surface becomes a Riemannian manifold with tension metric $\mathbf{g}(\xi)$. (We use italic letters like \mathbf{g} for continuous fields, and upright letters like τ_{ij} for discrete objects). The tension metric defines the (infinitesimal) tension between adjacent cells $\xi, \xi + d\xi$ as $d\tau = (\mathbf{g}(\xi)_{ab} d\xi_a d\xi_b)^{1/2}$. The connectivity of the cell array (i.e., which pairs of cells are adjacent) is represented by a second Riemannian metric $a_{ab}(\xi)$, defined so that the distance between adjacent cells is 1. The adjacency

metric \mathbf{a} corresponds to a triangulation where every edge has length 1.

We now summarize the key results of the “top-down” continuum analysis. First, a conformal embedding $\tau(\xi)$ of g into physical space defines an emergent, stress-free reference state (called $z(\xi)$ in the notation of the companion paper [11]). The conformal embedding defines isothermal coordinates: in τ -coordinates, g becomes isotropic, $g(\tau)_{ab} = \lambda_g^2(\tau)\delta_{ab}$ where the function λ is called the conformal factor. The intracellular pressure p is linked to λ_g and obeys a Poisson equation, sourced by the Gaussian curvature K of the tension metric:

$$p = p_0 \lambda_g \quad \Rightarrow \quad \Delta \log p = \lambda_g^2 K \quad (3)$$

where p_0 is the reference or average pressure.

Second, external forces lead to a displacement \mathbf{u} away from the emergent reference state. An emergent stress-strain relationship determines the resulting macroscopic tensile stress tensor $\boldsymbol{\sigma}$:

$$\boldsymbol{\sigma} = p \frac{R(\phi_I) \cdot \Sigma_F \cdot R(\phi_I)^T}{\det \Sigma_F} \quad (4)$$

Here, $F_{ab} = \delta_{ab} + \partial_a u_b$ is the deformation gradient (in the companion paper, F is denoted $\mathbf{D}w$, the differential of the map $w(z, \bar{z})$ from the reference configuration z to the physical configuration w .), and $F = R(\phi_I) \cdot \Sigma_F \cdot R(\phi_R)^T$ is its singular value decomposition (SVD) ($R(\phi)$ is a rotation matrix, and ϕ_I, ϕ_R are angles). To be compatible with mechanical balance, these deformations must take the form

$$\mathbf{u} = \nabla \theta + \mathbf{f} \quad (5)$$

where θ is a scalar potential and \mathbf{f} is a conformal vector field.

Third, adiabatic morphogenetic dynamics alter the tension metric, resulting in tissue flow. The change in \mathbf{g} can be decomposed into contributions from tension dynamics and from topological cell rearrangement, which correspond to changes in the adjacency metric \mathbf{a} . It was proposed that topological rearrangement is triggered by the total deformation from the adjacency metric to the physical configuration of the tissue.

Summary of key results

The present manuscript connects this effective theory with a “bottom-up” coarse-graining analysis of the ATN model. The overarching theme is to cast the constraints of local mechanical balance in geometric form, using the framework of discrete conformal maps. This both provides an elegant description at the cell level and makes the transition to the continuum seamless. Coarse-graining can calculate parameters of the effective theory from the cell-level “microstructure”, for example, the yield strain for cell rearrangement. We will gradually build up complexity.

In Sect. I, we start with the simplest case where intracellular pressures are all identical $p_i = p_0$. Here, the tension triangulation must be planar and is equivalent to the Maxwell-Cremona force tessellation. The *Voronoi dual* of the triangulation defines a force-balanced cell tessellation with vertex positions \mathbf{r}_{ijk} whose coarse-grained stress tensor is constant and isotropic, and can hence be balanced by a uniform pressure. The Voronoi dual of the tension triangulation, therefore, defines the macroscopically stress-free reference state of the tissue. However, tensile force balance only determines the relative orientation of cell interfaces, not their lengths. This gives rise to the *isogonal* soft mode: adding a discrete-gradient displacement $\mathbf{r}_{ijk} \mapsto \mathbf{r}_{ijk} + (\nabla \theta)_{ijk}$, parametrized by the *isogonal potential* θ_i , leaves edge orientations invariant. The isogonal mode is the cell-level origin of the curl-free mode $\nabla \theta$ of the continuum theory. By calculating how this deformation stretches and displaces the active force dipoles (cell edges), we confirm the emergent macroscopic constitutive relation Eq. (4). The isogonal potential θ_i defines the discrete Airy function for the tensile stress σ . Our argument establishes a discrete Legendre duality between tension nets and granular materials, where discrete Airy functions have been studied previously.

Sect. II generalizes to the case of non-zero pressure differentials. We show that the force balance constraints are invariant under discrete conformal (local Möbius) transformations, and via the Young-Laplace law, link pressure and conformal factor. This identifies the cell-level origin of the conformal mode \mathbf{f} of the continuum theory. The isogonal potential, a soft mode when cells are perfectly compressible and pressure constant, is now determined by bulk elasticity, encoded in the constitutive relation $P(a)$.

Sect. III uses the link between conformal maps and pressure to generalize our results to generic, non-planar tension triangulations. Such triangulations have a non-zero angle deficiency at vertices – the discrete counterpart to Gaussian curvature K . Angle deficiency acts as a source for pressure differentials, recovering a discrete version of Eq. (3). This generalizes von Neumann’s law for the pressure in an n -sided foam bubble. The (discrete) conformal deformation caused by the pressure field deforms the non-planar tension triangulation into the flat physical cell tessellation. We explain how the tension triangulation defines a (piecewise-linear) Riemannian manifold. In the continuum limit, the discrete conformal map converges to a smooth conformal embedding of the tension metric, which plays the role of the stress-free reference state in the continuum theory.

The technical workhorses of Sects. II and III are discrete conformal maps [15]. Via this powerful mathematical approach, we formulate a type of conformal symmetry that is exact at the cell level, and parameterize all possible mechanically balanced cell tilings [8].

Sect. IV concerns topological cell rearrangement (T1 processes). We show that the adjacency metric of the continuum theory corresponds, on the microscopic level,

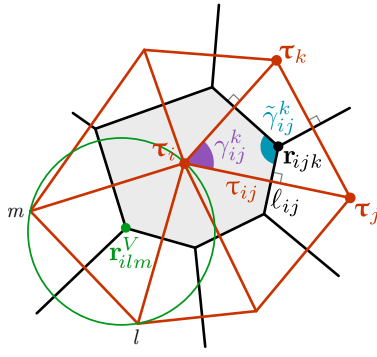


FIG. 2. ATN geometry and notation. Red: tension triangulation with vertices τ_i ; Black: cell tessellation with vertices τ_{ijk} . In mechanical balance, the angles $\tilde{\gamma}_{ij}^k + \gamma_{ij}^k = \pi$. Green: Voronoi vertices are triangle circumcircle centers.

to a discrete conformal embedding of the adjacency graph of the cell network. T1s, which remodel this graph, take place when cell interfaces shrink to length zero. This can occur either due to forces acting on the boundaries, thus driving the isogonal mode, or due to internal changes of tension. Exploiting the geometric framework, we calculate the yield strain and analyze its dependence on order parameters for the cell-level “texture”, linking macroscopic deformation to microstructure. The exact geometric “T1-threshold” justifies the phenomenological ansatz for topological dynamics presented in the companion manuscript.

Appendices A–H present technical details. In particular, tools from discrete differential geometry permit explicit connections between the discrete and continuum settings, summarized in Table I. Table II provides a list of symbols used in our notation.

RESULTS

I. TENSION NETWORKS WITH CONSTANT PRESSURE

Given the active tensions τ_{ij} , what is the physical configuration of the cell tessellation in force balance? This is the central question in the theory of active tension networks. To answer it, we first parameterize all tessellations compatible with microscopic force balance, and then compute their macroscopic stress.

A. Maxwell–Cremona tessellation and tension triangulation

We begin by casting the force balance condition Eq. (1) into a geometric form. First, the tensile forces at each tri-cellular vertex \mathbf{r}_{ijk} must sum to zero. Rotating each

force vector by $\pi/2$,

$$\tau_{ij}\mathbf{n}_{ij} + \tau_{jk}\mathbf{n}_{jk} + \tau_{ki}\mathbf{n}_{ki} = 0 \quad (6)$$

where $\hat{\mathbf{n}}_{ij}$ is the unit normal to interface ij at ijk . Hence, the tensile forces form a triangle with edge lengths $(\tau_{ij}, \tau_{jk}, \tau_{ki})$. These tension triangles fit together to form a dual *tension triangulation* with one node per cell (Fig. 2). Tension anisotropy corresponds to anisotropically shaped tension triangles. Geometrically, the corner angles $\tilde{\gamma}_{ij}^k$ of the tension triangle and the corresponding tricellular vertex angles γ_{ij}^k have to be complementary:

$$\tilde{\gamma}_{ij}^k + \gamma_{ij}^k = \pi \quad (7)$$

(Where necessary, tension triangulation quantities like $\tilde{\gamma}_{ij}^k$ are marked by a tilde.) Via the tension triangulation, the tensions τ_{ij} determine the relative orientations of cell-cell interfaces, so that tensile forces sum to 0 at each vertex.

For simplicity, we first consider the case where the intracellular pressures $p_i = p_0$ are constant, and, therefore, cell-cell interfaces are straight lines. In this case, the $\mathbf{n}_{ij} = \mathbf{n}_{ji}$ and the rotated force vectors $\tau_{ij}\mathbf{n}_{ij}$ fit together to form a planar *Maxwell–Cremona* tessellation. The Maxwell–Cremona tessellation defines a planar drawing/representation of the tension triangulation. As a consequence, in the constant-pressure case, the tension triangulation must be flat.

This Maxwell–Cremona construction is based solely on mechanical equilibrium and is also valid, for example, for a spring network in which tensions depend on the interface lengths. The key premise of the ATN model is that the τ_{ij} are instead determined by intrinsic motor molecule activity and independent of the ℓ_{ij} . (As we will see, the pressures p_i cannot be controlled independently. Instead, they are determined by passive bulk elasticity or incompressibility.)

B. From tensions to the physical configuration: Voronoi and Power tessellations

Since we assumed the tension triangulation is flat, we can find vertices τ_i in a common plane so that $\tau_{ij} = |\tau_i - \tau_j|$. We refer to these vertices as a drawing or *embedding* of the tension triangulation in the physical plane. The τ_i are the discrete counterpart of the isothermal τ -coordinates of the continuum theory: Indeed, one can define $\tau(\xi)$ by interpolation of $\tau_i = \tau(\xi_i)$. Because the tension between adjacent cells i, j is $\tau_{ij} = |\tau_i - \tau_j|$, the tension metric must be trivial, $g_{ab} = \delta_{ab}$.

Voronoi construction

We now construct a force-balanced reference state of the cell tessellation from the tension triangulation. Force

balance fixes the angles at the vertices in the cell tessellation, Eq. (7). We can fulfill this constraint by making junctions in the cell tessellation \mathbf{r}_{ij} orthogonal to the triangulation edges τ_{ij} [16]. Note that global orthogonality between tension edges and physical edges only holds for uniform pressure, as we will see below.

A geometrically natural choice is the Voronoi dual of the tension triangulation (see App. B). As we will see in the next section, the Voronoi tessellation is the macroscopically stress-free reference state for a given microscopic configuration of tensions. Voronoi cell vertices \mathbf{r}_{ijk}^V are the circumcenters of triangles (ijk) , which we scale by the *reference pressure* p_0^{-1} to convert units of line tension [N] to units of length [m]. In the remainder of the paper, we non-dimensionalize such that $p_0 = 1$. By construction, the Voronoi cell edges are orthogonal to their duals in the triangulation $\tau_{ij} \cdot (\mathbf{r}_{ijk}^V - \mathbf{r}_{ijl}^V) = 0$, thus guaranteeing force balance at cell vertices. A Voronoi cell C_i^V can equivalently be defined as the set of all points \mathbf{r} whose closest triangulation vertex is τ_i :

$$C_i^V = \{\mathbf{r} : |\mathbf{r} - \tau_i|^2 < |\mathbf{r} - \tau_j|^2 \forall i \neq j\} \quad (8)$$

The interface between two cells i, j is therefore the line $|\mathbf{r} - \tau_i|^2 = |\mathbf{r} - \tau_j|^2$. This distance-based construction makes it clear that the triangulation vertices τ_i become the Voronoi cell centroids \mathbf{r}_i^V . In the continuum, this allows us to identify an embedding $\tau(\xi)$ of the tension triangulation with the set of Voronoi cell positions

$$\mathbf{r}^V(\xi) = \tau(\xi) \quad (9)$$

The length ℓ_{ij} of an interface in quadrilateral $ijkl$ has a simple form in the Voronoi tessellation:

$$\ell_{ij} = \frac{1}{2} \tau_{ij} (\cot \gamma_{ij}^k + \cot \gamma_{ij}^l) \quad (10)$$

Physically, an edge must have non-negative length, $\ell_{ij} \geq 0$, leading to the *Delaunay condition* $\gamma_{ij}^k + \gamma_{ij}^l \leq \pi$ (geometrically, at $\gamma_{ij}^k + \gamma_{ij}^l = \pi$, the circumcircles of triangles ijk and ijl coincide). This condition plays an important role for T1 transitions [9, 17].

Isogonal mode and power tessellations

Fixing the orientations of all cell interfaces does not fully determine cell tessellation. A curl-free displacement of tri-cellular vertices will not rotate cell interfaces, keeping vertex angles fixed and thus preserving force balance [8, 18]. A curl-free displacement field is conveniently parametrized as the (discrete) gradient of a scalar potential θ_i ,

$$\mathbf{r}_{ijk} \mapsto \mathbf{r}_{ijk} + (\nabla_{\tau} \theta)_{ijk}, \quad (11)$$

where $(\nabla_{\tau} \theta)_{ijk}$ is the discrete gradient operator (App. A). Fig. 3 shows examples of isogonal deformations. Note that isogonal deformations preserve vertex

angles because they are irrotational. They are, however, *not* conformal. In fact, isogonal deformations generally cause shear. As they preserve vertex angles, such displacement fields have been termed *isogonal* [8], and we will refer to θ as the isogonal potential.

The existence of isogonal modes implies that for a single set of junctional tensions τ_{ij} , there is a whole family of force-balanced configurations, parametrized by θ_i . We use the Voronoi tessellation as a reference configuration for $\theta_i = 0$. We can now explicitly parametrize all force-balanced cell tessellations for a given tension triangulation as follows:

$$\mathbf{r}_{ijk}^I = \mathbf{r}_{ijk}^V + (\nabla_{\tau} \theta)_{ijk}. \quad (12)$$

The isogonal mode stretches and compresses interfaces, but does not rotate them (as one can verify using the definition of $(\nabla \theta)_{ijk}$ in App. A). The interface length ℓ_{ij}^I in a quadrilateral $ijkl$ is determined by a (discrete) second derivative of θ_i :

$$\ell_{ij}^I = \ell_{ij}^V + \hat{\mathbf{r}}_{ij} \cdot [(\nabla_{\tau} \theta)_{ijk} - (\nabla_{\tau} \theta)_{ijl}] \quad (13)$$

We refer to the condition $\ell_{ij}^I \geq 0$ as the *generalized Delaunay condition*.

The isogonal-mode construction is common in mathematics and computer graphics, where triangulations together with a dual tessellation (one vertex per triangle ijk so that triangulation and tessellation edges are orthogonal) are called “orthogonal duals” [19]. The generalized Voronoi construction for $\theta_i \neq 0$ is known in the literature under several names: Laguerre tessellations, (additively) weighted triangulations, and power diagram/tessellations [20]. We will use the latter term. In the power tessellation, a cell C_i^I is defined as the set of

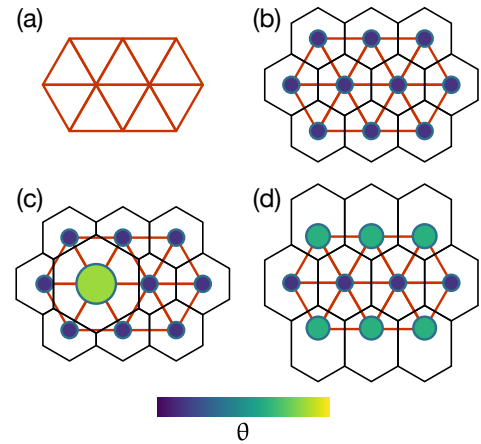


FIG. 3. Internal and boundary isogonal modes. (a) tension triangulation. (b) reference cell tessellation. (c) internal isogonal mode inflating a single cell without deforming the boundary of the cell patch. (d) global shear isogonal mode deforming the boundary. The radii of the vertex circle of the underlying decorated triangulation correspond to the values of the isogonal potential.

closest points under the generalized *power distance*

$$C_i^I = \{\mathbf{r} : |\mathbf{r} - \boldsymbol{\tau}_i|^2 - \theta_i < |\mathbf{r} - \boldsymbol{\tau}_j|^2 - \theta_j \forall i \neq j\} \quad (14)$$

Geometrically, the isogonal mode can be thought of as a *vertex circle* (sometimes also called *power circle*) of radius $\sqrt{\theta_i}$ around each vertex. One also refers to a triangulation together with a circle around every vertex as a *decorated triangulation* [21] (see Fig. 3).

The power distance measures the squared tangential distance from a point \mathbf{r} to the vertex circle. In this picture, the vertex \mathbf{r}_{ijk}^I can be constructed as the center of the face circle, the unique circle that intersects all vertex circles orthogonally (if $\theta_i = 0$, the face circle reduces to the circumcircle). Both definitions (discrete gradient and power distance [18, 20]) will become useful below, and are equivalent (App. B 1).

The discrete isogonal modes Eq. (12) provide the microscopic origin of the continuum curl-free mode $\nabla\theta$, with $\theta(\boldsymbol{\tau})$ defined by interpolation of the $\theta_i = \theta(\boldsymbol{\tau}_i)$. Note that microscopically, i.e. on the level of the cell vertices, the isogonal displacements are non-affine. In the continuum, we can write the isogonal deformation $\mathbf{r}_{ijk}^V \mapsto \mathbf{r}_{ijk}^V + (\nabla\theta)_{ijk}$ as a map $\mathbf{r}^V \mapsto \mathbf{r}^I = \boldsymbol{\tau} + \nabla_{\boldsymbol{\tau}}\theta(\boldsymbol{\tau})$. We define the isogonal deformation tensor

$$F_{ab}^I := \partial_{r_a} r_b^I(\mathbf{r}) = \delta_{ab} + \partial_{\tau_a} \partial_{\tau_b} \theta. \quad (15)$$

For future reference, we define the inverse of the isogonal map $\mathbf{r}^I \mapsto \boldsymbol{\tau}(\mathbf{r}^I) = \mathbf{r}^I + \nabla_{\mathbf{r}^I}\theta^*(\mathbf{r}^I)$. Its potential $\theta^*(\mathbf{r}^I)$ is given by the Legendre transform (which inverts the derivative of a function)

$$\frac{1}{2}|\mathbf{r}^I|^2 + \theta^*(\mathbf{r}^I) = \sup_{\boldsymbol{\tau}} [\mathbf{r}^I \cdot \boldsymbol{\tau} - \frac{1}{2}\boldsymbol{\tau}^2 - \theta(\boldsymbol{\tau})] \quad (16)$$

The inverse of the isogonal deformation tensor is therefore $(F^I)_{ab}^{-1} = \mathbb{I} + \partial^2\theta^*/(\partial r_a^I \partial r_b^I)$. To first order in $\nabla\theta$, one has $\theta^* \approx -\theta$.

C. Isogonal modes parametrize macroscopic self-stress

The large-scale mechanical state of the tissue is defined by the stress tensor σ , which we now relate to the microscopic configuration of tensions τ_{ij} and isogonal potential θ_i . Using the *Batchelor formula* [22] (also known as virial stress formula [23]), we can calculate a coarse-grained tensile stress-tensor for an area a , e.g., a cell,

$$\sigma = \frac{1}{a} \sum_{(ij) \in a} \ell_{ij} \tau_{ij} \hat{\mathbf{r}}_{ij} \otimes \hat{\mathbf{r}}_{ij}, \quad (17)$$

where each cell edge (ij) simply contributes a force dipole of strength $\ell_{ij}\tau_{ij}$. The total macroscopic stress is given by the sum of the tensile stress σ and the isotropic intra-cellular pressure (which we assumed constant):

$$\sigma^{\text{tot}} = \sigma - p_0 \mathbb{I} \quad (18)$$

Regular lattice

We begin with a periodic lattice composed of identical tension triangles with edges $\boldsymbol{\tau}_\mu$, $\mu = 1, 2, 3$, and cell edge vectors $\mathbf{r}_\mu = \ell_\mu \boldsymbol{\tau}_\mu^\perp / \tau_\mu$. Direct calculation (App. C 1) shows that the isogonal deformation tensor of the regular lattice reads

$$F^I = \frac{1}{2\tilde{a}} \sum_\mu \mathbf{r}_\mu \otimes \boldsymbol{\tau}_\mu^\perp = \frac{1}{2\tilde{a}} \sum_\mu \ell_\mu \tau_\mu \hat{\mathbf{r}}_\mu \otimes \hat{\mathbf{r}}_\mu \quad (19)$$

Thus, it differs from the Batchelor formula Eq. (17) only in the area-factor: \tilde{a} is the triangle area. Triangle and cell areas are related by $a = 2\tilde{a} \det F^I$, and therefore:

$$\begin{aligned} \sigma_{ab} &= \frac{F_{ab}^I}{\det F^I} = \epsilon^T \cdot (F^I)_{ab}^{-1} \cdot \epsilon \\ &= p_0 (\delta_{ab} + \epsilon_{ac} \epsilon_{bd} \partial_c \partial_d \theta^*) \end{aligned} \quad (20)$$

where we used the identity $M^{-1} = (\det M)^{-1} \epsilon^T \cdot M^T \cdot \epsilon$ for the inverse of 2×2 matrices. For clarity, in the final result, we have restored the dimensional factor p_0 , which sets the overall stress scale. This expression has the correct properties as a force-balanced continuum stress tensor: Symmetry, because isogonal displacement is curl-free, and force balance, because $\theta^*(\mathbf{r})$ defines the Airy stress function, $\partial_a \sigma_{ab} = (\partial_a \partial_c \epsilon_{ac})(\epsilon_{bd} \partial_d \theta^*) = 0$. The above calculation generalizes previous results for an ordinary fluid foam, where all τ_μ are equal to the foam surface tension [24].

A stress-free reference state is a central element of conventional elasticity theory. Equation (20) implies that σ^{tot} vanishes for $F^I = \mathbb{I}$. The reference pressure p_0 is exactly canceled by the local tensile stress, justifying the choice of p_0 as “unit conversion factor” from tension space to physical space. Indeed, by Eq. (1) the pressure balances the contractile tensions, $p_0 d\ell^2 \sim \tau d\ell$. Hence, the pressure sets the overall scale between tension and physical space, $p_0 \sim \tau/\ell$.

We conclude that the scaled Voronoi tessellation, dual to the embedding $\boldsymbol{\tau}_i$ of the tension triangulation, is a macroscopically stress-free reference state. This is equivalent to the finding in the continuum that an isometric embedding of the tension manifold defines a stress-free set of cell positions. Macroscopic stresses arise due to isogonal deformations, which move and stretch active force dipoles (cell edges). Eq. (20) plays the role of an effective stress-strain relationship with shear modulus p_0 , and recovers the continuum result Eq. (4) (the isogonal deformation tensor F^I is symmetric, so $F^I = R(\phi_I) \cdot \Sigma_F \cdot R(\phi_I)^T$ – hence the notation “ ϕ_I ”). Different isogonal modes thus correspond to different states of *macroscopic* self-stress. In contrast to states of self-stress in granular materials, these states differ in their geometry (cell shapes and areas) as illustrated in Fig. 3.

Importantly, in the Voronoi configuration, the macroscopic stress vanishes no matter how anisotropic the microscopic tension configuration is. Heuristically, this can

be justified by computing the traction force $\mathbf{f}_{ij} = \tau_{ij} \mathbf{n}_{ij}$ normal to an interface between two cells with centroids $\mathbf{r}_i, \mathbf{r}_j$. In the Voronoi state, $\mathbf{r}_i^V = \boldsymbol{\tau}_i$, and hence the force flux $|\mathbf{f}_{ij}|/||\mathbf{r}_{ij}| = \tau_{ij}/|\boldsymbol{\tau}_i - \boldsymbol{\tau}_j| = 1$ is isotropic and spatially constant (a continuum version of this argument is used in the companion paper). A thought experiment on a conventional 2D fluid foam illustrates the importance of distinguishing macroscopic stress and the microscopic configuration of tensions. Each interface in the foam is under surface tension. Nonetheless, cutting a freely floating bubble raft is macroscopically stress-free: cutting it does not lead to macroscopic recoil. Hence, the macroscopic configuration can be stress-free while microscopic stresses are nonzero. In living tissues, stresses at different scales can be assessed by different types of laser ablation (or cutting) experiments (see Discussion).

Eq. (20) generalizes previously known results for conventional fluid foams [12, 25]. In a foam with constant interfacial tension τ , the tension triangle area is $\tilde{a} = \sqrt{3}\tau^2/4$ and the hexagonal cell area is $a = 3\sqrt{3}\ell^2/2$, giving $p_0 = \tau/(\sqrt{3}\ell)$, recovering the literature result [12].

General triangulations: mechanical Legendre duality

We now generalize the above derivation from a regular lattice to an arbitrary tension network. To this end, we use an interpolation scheme used in finite element methods. This defines a principled way to transition between discrete values h_i at triangulation vertices and continuous functions $h(\boldsymbol{\tau})$. In App. A, we define piecewise affine barycentric interpolation functions $\phi_i(\boldsymbol{\tau})$, each with support only in the neighborhood of vertex i , $\phi_i(\boldsymbol{\tau}_j) = \delta_{ij}$. From this interpolation basis, one can derive discretizations of differential operators like the gradient (used in Eq. (12)) and the Laplacian. Applied to the stress tensor, the interpolation scheme computes the “stress flux” (traction force magnitude) σ_{ij} through an interface ij .

Since the barycentric interpolation scheme is defined on a triangulation, we first consider a “mechanical dual” in which the roles of tension space and physical space are reversed. One can, for instance, take the triangulation as a truss network (or as the contact pattern of a frictionless granular material), with “tension” ℓ_{ij} on each link [26]. This allows us to use barycentric interpolation to define a dual stress tensor $\tilde{\sigma}$ [27, 28] which we will argue is the inverse of the stress σ .

The force balance condition for the mechanical dual reads $\sum_{j \sim i} \ell_{ij} \hat{\boldsymbol{\tau}}_{ij} = 0$. This is simply the statement that the cell tessellation polygons are closed, so the dual is also in mechanical balance and must have a balanced stress tensor $\tilde{\sigma}$. In the mechanical dual, isogonal modes correspond to so-called “wheel moves”, which parameterize the set of self-stress states of a granular material [29].

Following Refs. [27, 28], we use barycentric interpolation to link the discrete dual force network to a continuum dual stress tensor. Details are presented in App. C 2. The key to the calculation is computing the ℓ_{ij} in terms

of θ_i . In the specific case $\theta_i = \text{const.}$, this yields $\tilde{\sigma} = \mathbb{I}$, that is, the dual stress for the Voronoi tessellation is constant and isotropic, analogous to our above finding for the physical stress σ . In general, one finds that the isogonal potential is the (discrete) Airy function for the dual stress $\tilde{\sigma}$ [28], so $\tilde{\sigma}$ is automatically balanced. In the continuum limit:

$$\tilde{\sigma}_{ab}(\boldsymbol{\tau}) = \epsilon_{ac}\epsilon_{bd}\partial_{\tau_c}\partial_{\tau_d}(\frac{1}{2}|\boldsymbol{\tau}|^2 + \theta(\boldsymbol{\tau})) \quad (21)$$

To relate $\tilde{\sigma}$ to the physical stress σ , compare the Batchelor formulas for the dual and primal stresses at a cell i :

$$\tilde{\sigma}_i = \frac{1}{\tilde{a}_i} \sum_{j \sim i} \ell_{ij} \frac{\boldsymbol{\tau}_{ij}}{2} \hat{\boldsymbol{\tau}}_{ij} \otimes \hat{\boldsymbol{\tau}}_{ij} \quad (22a)$$

$$\sigma_i = \frac{1}{a_i} \sum_{j \sim i} \tau_{ij} \frac{\ell_{ij}}{2} \hat{\boldsymbol{\tau}}_{ij}^\perp \otimes \hat{\boldsymbol{\tau}}_{ij}^\perp \quad (22b)$$

where \tilde{a}_i is the Voronoi area[30] of vertex i . Direct calculation yields $\tilde{\sigma}_i \cdot \sigma_i \propto \mathbb{I}$. Numerical checks for disordered triangulations confirm this relation and indicate that the proportionality factor is within $\sim 1\%$ of unity (see Fig. 13B–C). We therefore have (to good approximation)

$$\sigma(\mathbf{r}^I(\boldsymbol{\tau})) = \tilde{\sigma}^{-1}(\boldsymbol{\tau}) \quad (23)$$

Since the Legendre transform inverts the Hessian of a function, Eq. (23) implies that σ ’s Airy function must be the Legendre dual of Eq. (21), which is given by $\frac{1}{2}|\mathbf{r}^I|^2 + \theta^*(\mathbf{r}^I)$; Eq. (16). This confirms the lattice result Eq. (20).

The Legendre duality between dual and physical stress is natural, since the mechanical dual (interchanging the roles of $\boldsymbol{\tau}_{ij}$ and ℓ_{ij}) can be thought of as a Legendre transform. Specifically, the elastic energy differential of the cell tessellation $dE = \sum_{ij} \tau_{ij} d\ell_{ij}$ is Legendre transformed to $\sum_{ij} d(\tau_{ij} \ell_{ij}) - dE = \sum_{ij} \ell_{ij} d\tau_{ij}$. Interestingly, the Airy function $\frac{1}{2}|\mathbf{r}^I|^2 + \theta^*(\mathbf{r}^I)$ must be convex because of the purely contractile nature of the tensile stress (i.e., σ_{ab} is positive semi-definite). As we will discuss in Sec. IV, failure of convexity signals an instability to topological cell rearrangements due to the vanishing of interface lengths ℓ_{ij} . Cell rearrangements form a dynamic mechanism ensuring the convexity of the Airy function (and therefore, the well-definedness of the Legendre transform).

Interior and boundary isogonal modes

While all isogonal deformations preserve the vertex angles γ_{ij}^k , only deformations that leave the tissue boundary are true zero modes of the energy $dE = -\sum_{ij} \tau_{ij} d\ell_{ij} + p_0 \sum_i da_i$. Isogonal deformations of the tissue boundary generically change the energy – the tissue acts like an elastic material with stiffness p_0 . (See Fig. 3 for examples of interior and boundary isogonal modes).

Hence, the boundary modes are determined by the stress boundary conditions, for instance, stress-free boundaries. The Voronoi configuration corresponds to the absence of external forces. More generally, the isogonal mode can represent mechanically equilibrated states of the tissue in response to external forces because it respects the vertex force-balance constraint Eq. (6). Correspondingly, in the companion paper [11], the curl-free $\nabla\theta$ mode emerged from the solvability condition for the continuum force-balance equations.

In the interior, $\sigma \neq 0$ is possible even for free boundary conditions, as the interior isogonal modes are soft. A constraint on cell areas, e.g., incompressibility, is required to lift the degeneracy (see companion paper). Such a constraint elicits pressure differentials, to which we turn next.

II. TENSION NETWORKS WITH PRESSURE DIFFERENTIALS

A. Pressure gradients generate conformal deformations

Recall that the overall length scale of the cell tessellation is set by pressure–tension balance, $\ell \sim \tau/p$. This suggests that a *non-uniform* pressure field might act as a *local* scale factor. Indeed, force balance at the vertices of a tension network is a local angle constraint invariant under scaling and rotation of the cell tessellation, i.e., under conformal maps. A spatially varying scale factor bends cell interfaces. Normal force balance along the interface then requires a pressure difference across it (Young–Laplace law).

We now build on this intuition to show that a force-balanced cell tessellation with pressure gradients can be conformally mapped to a uniform-pressure cell tessellation. We can therefore parametrize cell states with the same tensions, but different pressures, by a conformal map (just like curl-free isogonal maps parameterize states with the same tensions, but different macroscopic stress). The Cauchy–Riemann equations for the conformal map turn out to be a continuum form of the Young–Laplace law.

To do so, we employ two pieces of mathematical “technology”, discrete conformal maps [15] and multiplicatively weighted Voronoi/power tessellations [8, 31]. This will generalize the results we obtained for constant pressure above, and provide the microscopic origin of the conformal mode of the continuum theory.

Conformal invariance of force balance

In the following, we represent the two-dimensional space in which the cell tessellation lies by the complex plane \mathbb{C} and identify coordinates (r_1, r_2) with complex numbers $z = r_1 + ir_2$. Conformal maps $z \mapsto f(z)$ locally

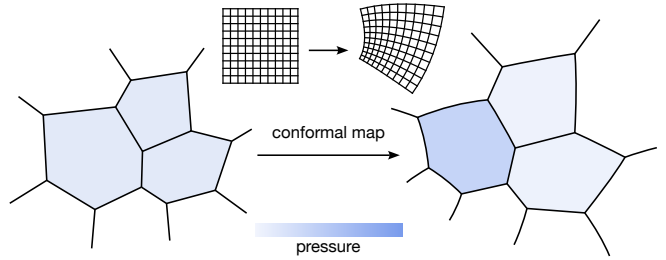


FIG. 4. A discrete conformal map of a polygonal cell tessellation produces a circular-arc polygonal (CAP) tiling. The discrete conformal map is parametrized by a scale factor for each cell, which is related to intracellular pressure via the Young–Laplace law.

rescale lengths by the conformal factor $\lambda_f = |\partial f / \partial z|$, but preserve angles.

The continuum theory identified conformal maps as soft modes of tension networks in the continuum limit. Let us therefore apply a conformal map $f(z)$ to a discrete cell tiling in the complex plane, keeping the tensions τ_{ij} fixed. Conformally deformed quantities are denoted by $(\cdot)^C$. We ask: is the deformed cell tiling in mechanical equilibrium, and if so, what are the corresponding pressures?

Tension force balance at vertices, Eq. (6), is trivially invariant, since a conformal map only rotates the local interface normals \mathbf{n}_{ij} . The cell-cell interfaces generally acquire line curvature κ_{ij} . Indeed, App. D 1 shows that conformally deforming a line with local normal \mathbf{n} changes its curvature κ as:

$$\kappa^C = \frac{\kappa}{\lambda} + \mathbf{n} \cdot \nabla \frac{1}{\lambda} \quad (24)$$

Normal force balance along the curved cell interfaces requires a pressure difference, determined by the Young–Laplace law

$$p_i - p_j = \kappa_{ij} \tau_{ij}. \quad (25)$$

Summing Eq. (25) around a vertex ijk (the discrete “curl”) results in a consistency equation for the curvatures at the vertex:

$$\tau_{ij} \kappa_{ij} + \tau_{jk} \kappa_{jk} + \tau_{ki} \kappa_{ki} = 0 \quad (26)$$

This equation implies that the curvatures must derive from a potential, namely, pressure. For example, curvatures that are all the same sign (a “spiral” shape) are not possible. Eq. (24) is the key to the conformal invariance of force balance, since it transforms as:

$$\sum_{\text{cyc.}} \tau_{ij} \kappa_{ij}^C = \frac{1}{\lambda} \sum_{\text{cyc.}} \tau_{ij} \kappa_{ij} - \left[\sum_{\text{cyc.}} \tau_{ij} \mathbf{n}_{ij} \right] \cdot \nabla \lambda^{-1} = 0 \quad (27)$$

The second term vanishes due to tension force balance Eq. (6). We conclude that Eqs. (26) and (6) are invariant under conformal maps they preserve force balance at vertices.

However, for a general conformal map, the curvature along a mapped interface is not constant (Eq. (24)): cell interfaces are not circular arcs. The Young–Laplace law (25) would therefore require intracellular pressure gradients. However, we assume that pressures are constant inside each cell (pressure equilibrates rapidly through cytoplasmic flows). As a consequence, cell interfaces must be circular arcs, and continuous conformal maps f are not admissible force-balance preserving modes on the discrete level.

Global Möbius transformations

To resolve this issue, we consider a special type of conformal maps: Möbius transformations (MTs) $M(z) = (az+b)/(cz+d)$ – compositions of scale-rotations $z \mapsto az$, translations $z \mapsto z + b$, and inversions $z \mapsto 1/z$ (the complex coefficients are conventionally normalized $ad - bc = 1$). MTs are the only conformal maps which map circles to circles, as one can easily verify for these “elementary” transformations (straight lines are considered as generalized circles through $z = \infty$, the “point at infinity”). Moreover, as conformal maps, MTs preserve circle intersection angles.

Applying an MT to a Voronoi tessellation yields a tessellation of circular arc polygons with the same vertex angles as the original tessellation (Fig. 5). By the argument of the preceding section, this tiling is in mechanical balance. Because the interfaces are circular arcs, the pressure inside each cell is constant. Therefore, MTs are bona fide soft modes at the discrete level.

Overall, these results suggest that force-balanced cell tessellations with a fixed set of tensions, but different cell pressures, can be mapped into one another via conformal transformations. However, continuous conformal maps do not respect local force balance, while a global MT (6 real parameters) is clearly insufficient to parametrize the extensive set of cellular pressures. Hence, we require a “local” Möbius symmetry.

B. Discrete conformal maps

We begin by studying the Voronoi case where all $\theta_i = 0$. To define a “local” MT, we draw on the notion of a *discrete conformal map* studied in the mathematics and computer graphics literature (reviewed in [32]). A continuous conformal map locally rescales lengths by an isotropic conformal factor λ . Discrete conformal maps define an analogous notion for maps between discrete surfaces, i.e., triangulations. A discrete conformal map is defined by a set of per-vertex scale factors λ_i [15]. The map rescales the length τ_{ij} of each edge ij as

$$\tau_{ij} \mapsto \tau_{ij}^C = \sqrt{\lambda_i \lambda_j} \tau_{ij}, \quad (28)$$

Note that an arbitrary set of scale factors λ_i results in a non-planar triangulation. We will return to this in

Sect. III.

Discrete conformal maps aim to reproduce as many features of the smooth theory as possible. For example, the composition of two discrete conformal maps is again discrete conformal. However, not all aspects can be preserved: a discrete conformal map does *not* preserve angles in the triangulation.

A key example of a discrete conformal map is an MT $M(z)$ of the plane. In this case, the scale factors are given by evaluating the conformal factor $M' = \partial M / \partial z$ at the triangulation vertices τ_i , $\lambda_i = |M'(\tau_i)|$. Indeed, the property

$$\begin{aligned} \tau_{ij}^C &= |M(\tau_i) - M(\tau_j)|^2 \\ &= |M'(\tau_i)M'(\tau_j)| \cdot |\tau_i - \tau_j|^2 \\ &= \lambda_i \lambda_j |\tau_i - \tau_j|^2 \end{aligned} \quad (29)$$

is easily verified for the only non-trivial MT $M(z) = 1/z$. A discrete conformal map of a triangulation can, in fact, be defined as a set of triangle-wise MTs M_{ijk} . In a quadrilateral $ijkl$, they must fit together so the scale factors λ_i are consistent [21]:

$$|M'_{ijk}(\tau_i)| = |M'_{ijl}(\tau_i)| \quad (30)$$

This alternative definition is equivalent to Eq. (28). Discrete conformal maps furnish a finite-element-like discretization of smooth conformal maps, analogous to the approximation of a continuous function by triangle-wise linear interpolation (App. A).

Multiplicatively-weighted Voronoi tessellations

So far, we have defined a discrete conformal map on a triangulation. However, we are interested in applying such a map to the dual cell tessellation (to our knowledge, this has not been studied in the mathematics literature).

To make this idea precise, we use *multiplicatively weighted Voronoi tessellations* (MWVTs, also known as circular Voronoi or Dirichlet partitions [7, 33]). MWVTs construct a circular arc polygonal (CAP) tessellation from a set of seed points τ_i^C and multiplicative weights λ_i . This notation anticipates that the seed points will be the image of the tension vertices τ_i under a discrete conformal map [15] with conformal factors λ_i . A MWVT cell i is defined as the set of points \mathbf{r} in the plane closest to vertex τ_i^C , using a multiplicatively weighted (“conformal”) distance

$$C^C = \{\mathbf{r} : \lambda_i^{-1}|\mathbf{r} - \tau_i^C|^2 < \lambda_j^{-1}|\mathbf{r} - \tau_j^C|^2 \forall i \neq j\} \quad (31)$$

Hence, $\lambda_i = 1$ recovers the Voronoi tessellation. Vertices are generically threefold. Interfaces ij are defined by the locus $\lambda_i^{-1}|\mathbf{r} - \tau_i^C|^2 = \lambda_j^{-1}|\mathbf{r} - \tau_j^C|^2$, and therefore, are Apollonian circles which intersect $\tau_i^C - \tau_j^C$ orthogonally. From the Apollonian circle property, it follows that the

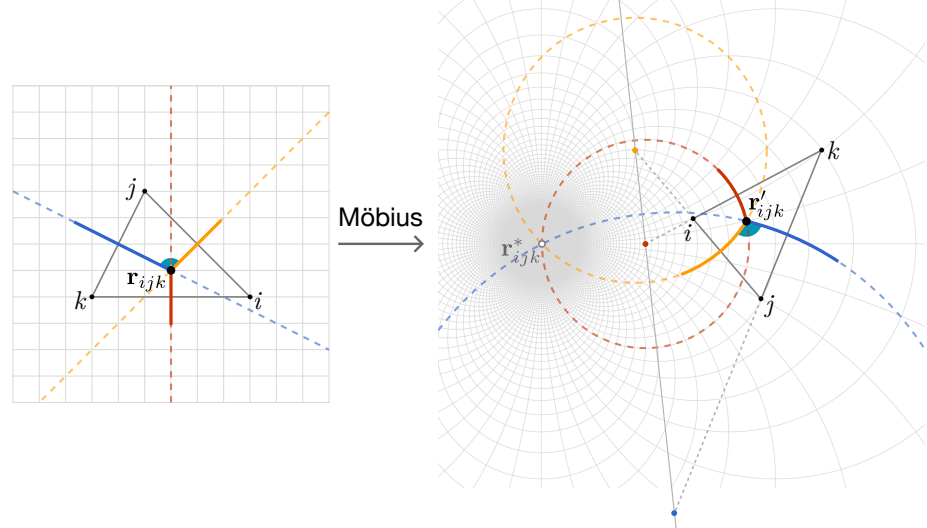


FIG. 5. Möbius transformation of a triangle and the dual Voronoi edges (colored) and vertex \mathbf{r}_{ijk} . The straight Voronoi edges become circular arcs. When completed, these circles meet in \mathbf{r}_{ijk}^* , the image of the point at infinity. Since the three circles intersect in two points, their centers lie on a straight line.

MWVT arcs have curvatures:

$$\kappa_{ij} = \frac{\lambda_i^{-1} - \lambda_j^{-1}}{|\boldsymbol{\tau}_i^C - \boldsymbol{\tau}_j^C|/\sqrt{\lambda_i \lambda_j}} = \frac{\lambda_i^{-1} - \lambda_j^{-1}}{\tau_{ij}} \quad (32)$$

Thus, the MWVT cells obey the Young–Laplace law Eq. (25) for pressures $p_i = 1/\lambda_i$ and tensions $\tau_{ij} = |\boldsymbol{\tau}_i^C - \boldsymbol{\tau}_j^C|/\sqrt{\lambda_i \lambda_j}$. The relation between $\tau_{ij}^C = |\boldsymbol{\tau}_i^C - \boldsymbol{\tau}_j^C|$ and τ_{ij} is exactly the defining property Eq. (28) of a discrete conformal map. Eq. (32) can also be seen as the discrete analogue of Eq. (24) for smooth conformal maps.

Local Möbius invariance of force balance

MWVTs are closed under MTs: applying an MT $M(z)$ to the vertices and edges of an MWVT results in another MWVT, with seed points $M(\boldsymbol{\tau}_i^C)$, weights $|M'(\boldsymbol{\tau}_i^C)|\lambda_i$, and tricellular vertices $M(\mathbf{r}_{ijk})$ [33]. This property follows because MTs preserve circles and their intersection angles. Hence, MWVTs behave exactly in the same way under MTs as discrete conformal maps.

This Möbius invariance allows showing that the MWVT cells also obey tension force balance at tricellular vertices, Eq. (7). To this end, we find an MT that locally maps an unweighted, straight-edge Voronoi tessellation onto a given MWVT (Fig. 5; see App. E 1 for details). Since the MT preserves vertex angles, the MWVT vertex angles γ_{ij}^k are indeed complementary to the angles $\tilde{\gamma}_{ij}^k$ of the corresponding tension triangulation $\tau_{ij} = |\boldsymbol{\tau}_i^C - \boldsymbol{\tau}_j^C|/\sqrt{\lambda_i \lambda_j}$. Therefore, while triangulation angles change under discrete conformal maps, tessellation angles are exactly preserved.

Taken together, we generalized the global Möbius invariance encountered above to a local invariance under

arbitrary (discrete) conformal maps. An example of a discrete conformal map that is not globally Möbius is shown in Fig. 14. On the level of the triangulation, discrete conformal maps act as a rescaling $\tau_{ij}^2 \mapsto \lambda_i \lambda_j \tau_{ij}^2$, while on the level of the dual tessellation, it acts as a local MT and determines the pressures $p_i = \lambda_i^{-1}$. We showed that these two actions are precisely compatible. Overall, we confirmed the intuition that pressure geometrically acts as a local scale factor.

C. Multiplicatively weighted power tessellations

We now generalize discrete conformal maps and multiplicatively weighted tessellations to the case of non-zero isogonal mode $\theta_i \neq 0$. Recall that the isogonal mode can be seen geometrically as a set of “power circles” with radius $\sqrt{\theta_i}$ and centers $\boldsymbol{\tau}_i$ (a “decorated triangulation”). Applying an MT to the power circles yields a new set of power circles. For example, $M(z) = 1/z$, changes circle centers and radii as $\boldsymbol{\tau}_i \mapsto \boldsymbol{\tau}_i^{\text{PC}} = \boldsymbol{\tau}_i/(|\boldsymbol{\tau}_i|^2 - \theta_i)$, $\sqrt{\theta_i} \mapsto \sqrt{\theta_i^{\text{PC}}} = \sqrt{\theta_i}/(|\boldsymbol{\tau}_i|^2 - \theta_i^2)$ [34]. In the decorated case, one Möbius-transforms vertex circles instead of vertex points. We can now generalize the machinery of the previous section: A discrete conformal map of a decorated triangulation and the associated power tessellation is a triangle-wise MT. Details are provided in App. E 2.

Decorated conformal maps correspond to a dual Multiplicatively weighted power tessellation (MWPT). MWPTs generalize power tessellations (Sect. 1B) by a multiplicative weight. A cell i is defined as the set of closest

points under the distance

$$\begin{aligned} C^{\text{PC}} = \{ \mathbf{r} : & \lambda_i^{-1}(|\mathbf{r} - \boldsymbol{\tau}_i^{\text{PC}}|^2 - \theta_i^{\text{PC}}) \\ & < \lambda_j^{-1}(|\mathbf{r} - \boldsymbol{\tau}_j^{\text{PC}}|^2 - \theta_j^{\text{PC}}) \forall i \neq j \} \end{aligned} \quad (33)$$

The arguments of the preceding section carry over to MWPTs: interfaces are circular arcs, the vertex angles are complementary to the tension triangulation τ_{ij} , and MWPTs transform under MTs according to a (decorated) discrete conformal map. Explicit calculation [7] shows that the curvatures κ_{ij} satisfy the the Young-Laplace law for cellular pressures $p_i = \lambda_i^{-1}$.

MWPTs, therefore, describe the image of a cell tessellation with nonzero isogonal deformation under a discrete conformal map, and are in mechanical balance. Like in the constant-pressure case, the isogonal modes parametrize the cell states constrained by tension force balance. However, isogonal modes are no longer zero modes but have an energy cost determined by pressure differentials $\sim \int p(\mathbf{r}) \Delta\theta(\mathbf{r}) d^2r$.

MWPTs parametrize all mechanically balanced states

Taking a step back, we have constructed a series of successively more general force-balanced tessellations: Voronoi, power, multiplicative Voronoi, and, finally, multiplicative power tessellations. We have connected MWPTs to discrete conformal maps of the tension triangulation, elucidating the link between geometry and mechanics, summarized in Fig. 6. The resulting theory allows us to solve the “forward problem”, namely, constructing the cell tessellation given the intrinsic active tensions. The connection to discrete conformal maps also allows us to naturally coarse-grain to the continuum in Section II E.

Refs. [7, 31] originally introduced MWPTs (without the link to discrete conformal maps) to parametrize force-balanced states of cell tessellations in the context of the corresponding inverse problem. They showed how to construct the MWPT from a given cell geometry (vertex positions \mathbf{r}_{ijk} and curvatures κ_{ij}). This can be used to infer interfacial tensions and pressures from microscopy data. Ref. [31] showed that any cell tessellation tension-pressure force balance is an MWPT. Hence, MWPTs exhaust all mechanically relevant cell geometries.

This can be seen by comparing geometric degrees of freedom with force-balance constraints. By Euler’s polyhedra formula, the numbers C, E, V of cells, edges, and vertices of the cell tessellation obey $C - E + V = 2$, and hence $E \approx 3C, F \approx 2C$. A generic circular-arc polygonal tessellation has $3E = 9C$ d.o.f.s, the 2D-centers and radii of the circular arcs. Force balance at vertices and across edges (Young-Laplace) implies $V + E = 5C$ constraints, leaving $4C = E + C$ d.o.f.s, precisely the number specified by the MWPT seed points and weights $(\boldsymbol{\tau}_i^{\text{PC}}, \lambda_i, \theta_i)$. We emphasize, however, that the discrete-conformally deformed triangulation $\boldsymbol{\tau}_i^{\text{PC}}$ is an intermediate step in the construction of the cell tessellation that

does not have direct physical significance. The control parameters in an MWPT are instead the tensions τ_{ij} and the isogonal potential θ_i . (As we will see below, the λ_i are determined by τ_{ij}, θ_i up to boundary values, much like a continuous conformal map is determined by its boundary values. They do not contribute additional bulk degrees of freedom.).

D. Bulk elasticity and external forces determine isogonal modes

Physically, in the ATN model, the tensions τ_{ij} are set intrinsically by motor molecule concentration. By contrast, the isogonal potential is determined by passive bulk elasticity, encoded in the constitutive equation of state $P(a)$ that relates pressure p to cell area a (we emphasize that the link $p_i = \lambda_i^{-1}$ between pressure and conformal factor is not, in itself, a constitutive equation). For instance, if cells are incompressible, $a_i = a_0$ everywhere. These C constraints can be fulfilled by the C isogonal potentials θ_i . More generally, for an arbitrary equation of state, the requirement $p_i = p(a_i)$ selects the physical state(s) among all MWPTs for a given tension triangulation.

If, on the other hand, individual cells are fully compressible, the isogonal mode is an unconstrained soft mode, the case studied in Ref. [8]. (A global, constant pressure is instead provided through a total area constraint.). In the fully compressible case, conformal deformations are not possible. Eq. (36) prescribes how pressures must change under conformal maps to maintain force balance. To generate this pressure, cells must have a non-vanishing compressibility.

E. Pressure, stress, and conformal maps in the continuum limit

In the continuum limit, a discrete conformal map λ_i converges towards a conformal map $z \mapsto z^C = f(z)$, with conformal factor $\lambda(\mathbf{r})$. Above, we showed that a discrete conformal map preserves force balance. This property carries over to the continuum [35]. In fact, one can show this without reference to the specific microscopic structure we have assumed here [11].

Young-Laplace law links pressure and conformal factor

Let us re-derive the link between the conformal factor and the corresponding pressure in the continuum limit. This link ultimately arises from the Cauchy-Riemann (CR) equations for the conformal map. In particular, the CR equations link the conformal factor $\lambda_f = |\partial f / \partial z|$ and the vorticity $\omega = \arg[\partial f / \partial z]$. The CR equations for

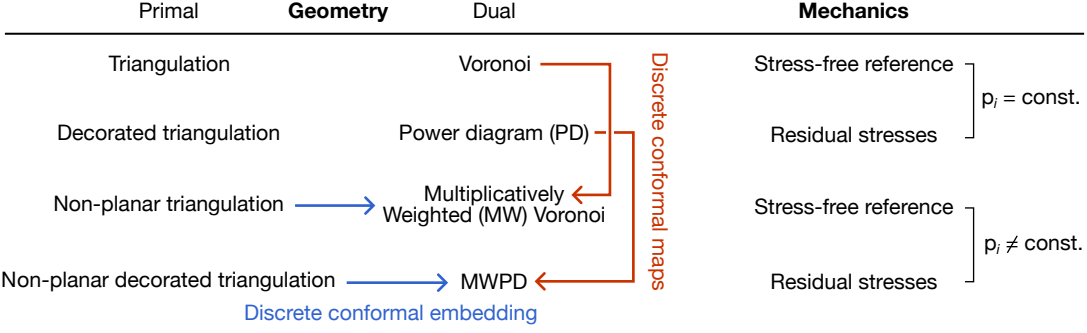


FIG. 6. Connections between discrete geometry (generalized Voronoi tessellations) and the mechanical states they represent. Note: Discrete conformal maps and embeddings are piecewise Möbius, parametrized by scale factors at triangle vertices.

$\log \partial_z f = \log \lambda + i\omega$ read:

$$\partial_a \log \lambda = \epsilon_{ab} \partial_b \omega. \quad (34)$$

Eq. (34) plays the role of a continuum form of the Young–Laplace law: curvature (a gradient in vorticity) is balanced by a gradient in pressure (conformal factor) along the orthogonal direction.

To make the connection with the cell-level, we combine Eq. (24) with the Young–Laplace law Eq. (25):

$$\begin{aligned} \mathbf{n}_{ij} \cdot \nabla_{\tau} p(\tau) &\approx \frac{p_i - p_j}{\tau_{ij}} = \kappa_{ij} \approx \mathbf{n}_{ij} \cdot \nabla \lambda^{-1}(\mathbf{r}^I) \\ \Rightarrow \nabla p/p_0 &= (F^I)^{-1} \nabla \lambda^{-1} \end{aligned} \quad (35)$$

where we used the relation $\nabla_{\tau} = F^I \nabla$ for the coordinate transformation from τ to \mathbf{r}^I . For clarity, we have restored the dimensional factor p_0 . Eq. (35) implies a particularly simple result in the Voronoi state, where $F^I = \mathbb{I}$, namely $p = p_0/\lambda$. This matches the analysis of the multiplicatively weighted Voronoi tessellations from above, as well as the Eq. (3) of the continuum theory. (Note that the tension metric \mathbf{g} is a contravariant tensor, and therefore transforms like $\lambda_g = \lambda_{f^{-1}} = 1/\lambda_f$.)

Eq. (35) is solved by

$$p(\mathbf{r}' + \nabla \theta^*) = \frac{p_0}{\lambda(\mathbf{r}')}, \quad (36)$$

Physically, the isogonal displacement “advects” the pressure away from its Voronoi reference value $p = p_0/\lambda$. For an isogonal displacement that is small compared to the $\nabla \lambda$, one can approximate

$$p(\mathbf{r}) \approx \frac{p_0}{\lambda(\mathbf{r})} (1 - \nabla \lambda \cdot \nabla \theta). \quad (37)$$

To the best of our knowledge, this identification of conformal factor and pressure has not been recognized in previous works on foams.

Macroscopic stress tensor with pressure differentials

How does the conformal transformation change the macroscopic stress? By the Batchelor formula Eq. (17),

the tensile stress σ is given by the sum over local force dipoles, the cell-cell edges, each with magnitude $\sim \tau \ell/a$ and orientation $\hat{\mathbf{r}} \otimes \hat{\mathbf{r}}$. Hence, σ rotates covariantly and scales as $1/\lambda$ (precisely like the Laplace pressure inside a foam bubble). Using Eq. (20), the stress tensor of the conformally deformed cell tessellation thus reads:

$$\sigma = \frac{p_0}{\lambda} \frac{R^C \cdot F^I \cdot (R^C)^T}{\det F^I} \quad (38)$$

The stress has a simple expression in terms of the total deformation tensor F . Let us write $F = F^C \cdot F^I = R^C \cdot (\lambda F^I)$, where $R^C = F^C/\lambda$ is the conformal rotation matrix. Comparing this factorization with the singular value decomposition $F = R(\phi_1) \cdot \Sigma_F \cdot R(\phi_R)^T$, yields, after a few algebraic steps:

$$\sigma = p_0 \frac{R(\phi_1) \cdot \Sigma_F \cdot R(\phi_1)^T}{\det \Sigma_F} \quad (39)$$

This is precisely the result Eq. (4) of the continuum theory, but now obtained by coarse-graining the microscopic stress tensor.

The total stress $\sigma^{\text{tot}} = \sigma - p\mathbb{I}$ vanishes when $\theta = \text{const.}$. Hence, a configuration without isogonal displacement remains stress-free even in the presence of cell pressure gradients (there are no macroscopic pressure gradients, however, since $\sigma^{\text{tot}} = 0$). In App. D 2 we verify that force balance, $\text{div } \sigma^{\text{tot}} = 0$, is guaranteed because F^I derives from a potential, p is linked to λ via Eq. (35), and the λ and ω are linked through the Cauchy–Riemann equations (34). For small isogonal and conformal displacements $\nabla \theta$, $f(z) - z$, we can expand Eq. (38) to linear order. One finds that

$$\sigma_{ab}^{\text{tot}} \approx -p_0 \epsilon_{ac} \epsilon_{bd} \partial_c \partial_d \theta. \quad (40)$$

The conformal mode does not contribute to the large-scale stress. Microscopically, f changes cellular pressure and isotropic tensile stress, but these are indistinguishable in the continuum.

In summary, pressure gradients correspond to conformal deformations of the cell tessellation, and vice versa. In the next section, we will use this relation to generalize our theory to non-planar tension triangulations.

III. NON-PLANAR TENSION TRIANGULATIONS AND PRESSURE DIFFERENTIALS

A. Discrete curvature: the angle deficit

So far, we have assumed a flat tension triangulation. However, in general, a triangulation specified through its adjacency and the edge lengths cannot be isometrically embedded in the plane. The elementary obstruction to flatness is the *angle deficit* of the plaquette around a vertex (Fig. 7b)

$$\delta_i = 2\pi - \sum_{(jk) \sim i} \tilde{\gamma}_{jk}^i \quad (41)$$

This angle deficit implies a concentration of Gaussian curvature at the vertex, $K_i = \delta_i/a_i$.

Mechanically, a non-planar tension triangulation means that tensions alone cannot be in global force balance in the plane – pressure differences are required. Force balance at the vertices implies that the angles at which cell interfaces meet are complementary to the triangle angles, $\gamma_{jk}^i - \pi = -\tilde{\gamma}_{jk}^i$ (Eq. (7)). Hence,

$$\delta_i = 2\pi - \sum_{jk} \tilde{\gamma}_{jk}^i = 2\pi - n\pi + \sum_{jk} \gamma_{jk}^i \quad (42)$$

where n is the number of neighbors of i . For a straight-edge polygon, $\sum_{jk} \gamma_{jk}^i = n\pi$, so the only way to compensate for the angle deficit in the plane is to curve the cell interfaces:

$$\delta_i = \oint \kappa d\ell = \sum_j \ell_{ij} \kappa_{ij} \quad (43)$$

since $\ell_{ij} \kappa_{ij}$ is the rotation angle of the tangent vector along the (circular arc) interface ij . Gaussian curvature of the tension triangulation (i.e., non-planarity, $\delta_i \neq 0$) thus implies line curvature of the planar cell interfaces and requires pressure differences between cells [8]. For example, in a conventional 2D fluid foam, a 5-sided cell is under higher pressure while a 7-sided cell is under lower pressure (the angle deficit being $\pm\pi/3$). Diffusion of gas driven by these pressure differences gives rise to the famous von Neumann law governing the coarsening of a 2D foam.

In this section, we systematically consider the implications of the angle deficit for generalized foams, using the technology of (discrete) conformal maps developed in the preceding section. We conformally deform the non-planar tension triangulation to flatten it. Once this is accomplished, we can construct the dual, force-balanced cell tiling using multiplicative weighted tessellations.

B. Continuous and discrete conformal maps on curved surfaces

How can we construct such a conformal “flattening” map? For flat conformal maps (i.e., to and from the

plane), Eq. (34) implies that $\log \lambda$ must be a harmonic function, $\Delta \log \lambda = 0$. More generally, a conformal map between two (curved) Riemannian surfaces with metrics \mathbf{g}, \mathbf{g}^C rescales the metric, $\mathbf{g}^C = \lambda^{-2} \mathbf{g}$, where the λ is the conformal factor. The resulting change in Gaussian curvature K reads [36]:

$$K^C = \lambda^2 K + \Delta \log \lambda \quad (44)$$

where Δ is the Laplace–Beltrami operator. In particular, a conformal map to the plane must fulfill the Liouville equation $-\lambda^{-2} \Delta \log \lambda = K$. The *uniformization theorem* states that this Poisson-like equation has a solution, unique up to scale: any curved 2D surface can be conformally mapped to the plane (provided it is topologically equivalent to a disk).

The discrete equivalent of the curvature is the angle deficit at the vertices. By calculating how the angles of a triangle change as its sidelengths are rescaled, Ref. [15] showed that the change in discrete curvature due to a small discrete conformal deformation $d\lambda_i$ reads:

$$(\Delta d \log \lambda)_i = -d\delta_i \quad (45)$$

Here, Δ is a finite-element-like discrete Laplace operator. Indeed, the Laplacian of a discrete function h_i on a triangulation can be calculated via the divergence formula (App. A 1):

$$\begin{aligned} \int_i \Delta h \, da &= \int_i \operatorname{div}(\nabla h) \, da = - \int_{\partial i} \nabla h \cdot \mathbf{n} \, d\ell \\ &\approx \sum_{j \sim i} \ell_{ij} \frac{h_j - h_i}{\tau_{ij}} := (\Delta h)_i \end{aligned} \quad (46)$$

By integrating (45), one can prove a discrete uniformization theorem. For any triangulation topologically equivalent to a disk, one can find a set of vertex scaling factors λ_i , unique up to scale, so that the rescaled triangulation has zero angle defect and can be drawn in the plane. (We implicitly assume the Delaunay condition is fulfilled). This theorem also holds for decorated (i.e., $\theta_i \neq 0$) discrete conformal maps [21].

C. Tension-triangulation curvature sources pressure gradients

We can therefore find a set of scaling factors λ_i that conformally embed the tension triangulation τ_{ij} into the plane, i.e., as a set of 2D vertices τ_i^C . This discrete conformal embedding is equivalent to the isothermal coordinates for the tension manifold used in the continuum theory. As we showed in the preceding section, from the planar τ_i^C triangulation, we can construct the cell tessellation as a multiplicatively weighted tessellation with pressures $p_i = \lambda_i^{-1}$. By Eq. (45), the pressure therefore obeys a discrete Poisson equation with the angle deficit as source term, $(\Delta \log p)_i = -\delta_i$.

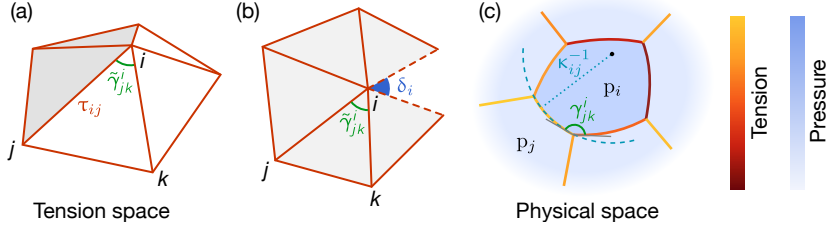


FIG. 7. Curvature of the tension triangulation (a) is revealed through the angle deficit that appears when “flattening” a plaquette (b). In physical space, this implies pressure gradients because the angle deficit must be accommodated by line curvatures κ_{ij} in the plane (c). (Note that the curved triangulation (a) is drawn in 3d space for illustration purposes; the theory does not make use of an embedding in 3D).

Indeed, this Poisson equation can be derived directly from the Young–Laplace law. We consider an infinitesimal deviation from uniform pressure $p_i = 1 + dp_i$. We start from Eq. (43). The curvatures κ_{ij} are determined by the pressures via the Young–Laplace law:

$$\begin{aligned} \delta_i &= \sum \ell_{ij}^C \kappa_{ij} \approx \sum \ell_{ij} \frac{p_i - p_j}{\tau_{ij}} \\ &\approx \sum \ell_{ij} \frac{\log p_i - \log p_j}{\tau_{ij}} = (\Delta \log p)_i \end{aligned} \quad (47)$$

To linear order, we replaced the edge lengths by their undeformed value $\ell_{ij}^C = \ell_{ij} + \mathcal{O}(dp_i)$. The result can be recognized as the discrete Laplacian Eq. (46). Therefore, the pressure field obeys a discrete Poisson equation in which the angle deficit appears as a source term:

$$(\Delta \log p)_i = -\delta_i \quad (48)$$

Eq. (48) is a discrete version of Eq. (3) obtained in the continuum analysis, and generalizes the von Neumann law for an ordinary foam discussed above. By Eq. (48), the pressure field/conformal factor has no bulk degrees of freedom – it is determined by its boundary values (in the absence of external forces, we use $p_i = 1$ as a boundary condition, corresponding to the discrete conformal embedding with minimal distortion). Put another way, a cell cannot change its pressures and tensions independently in mechanical equilibrium.

Note that the discrete Laplace operator Eq. (46) depends on the cell edge lengths ℓ_{ij} , which are stretched and compressed by the isogonal mode. For instance, if a cell is isogonally inflated, its interfaces elongate, and a smaller curvature/pressure gradient suffices to compensate for the same angle deficit (see Fig. 17). In the continuum, the discrete Laplace operator corresponds to an anisotropic, weighted “isogonal” Laplacian Δ^I . In App. F, we argue that Δ^I has a natural interpretation as a deformed Laplace–Beltrami operator, and explain the continuum limit of isogonal modes on non-flat triangulations.

D. From a non-planar triangulation to a Riemann surface

Given conformal factors/pressures λ_i which solve Eq. (45), we can embed the conformally deformed tension triangulation τ_{ij}^C in the plane, i.e., find tension vertices τ_i^C with $\tau_{ij}^C = |\tau_i^C - \tau_j^C|$. This way, even non-flat triangulations can be embedded in the plane, albeit with conformal distortion. Then, the physical cell tiling is constructed as the corresponding MWPT.

This procedure can be given an alternative interpretation, which makes the role of the isogonal potential more transparent. As noted above, a triangulation, specified by edge lengths τ_{ij} and the adjacency graph, defines a Riemannian surface. This statement is particularly obvious if the triangulation is flat, but it holds more generally. A manifold is defined by a set of local coordinate charts and transition functions between them [36]. In a triangulation, each quadrilateral $ikjl$ (i.e., pair of adjacent triangles) can be isometrically embedded in the plane, flattening the “hinge” between them [19]. This defines the charts. Within each, the metric is Euclidean. The transition maps are defined by two overlapping quadrilaterals and are linear. Even though the triangulation looks “kinked” when drawn in 3D, intrinsically, it defines a smooth Riemannian manifold (Except at the vertices, which can form cone singularities. These singularities pose no problem since they are “isolated”, and can be removed by local smoothing). Overall, this procedure explains how the tension triangulation defines the tension manifold and metric used in the continuum theory.

Via the hinge map, the construction of the Voronoi dual and isogonal displacements generalizes easily to non-flat triangulations: One performs the geometric constructions in the plane of each triangle separately [18] as illustrated in Fig. 8. Each Voronoi vertex is found as the circumcenter in the plane of the corresponding triangle. Thanks to the hinge map, the resulting tessellation of “kinked polygons” (green and purple lines in Fig. 8) is consistent across neighboring triangles.

To obtain a physical cell tessellation (in flat space) from this non-planar cell tessellation, one applies a discrete conformal map. Because a conformal deforma-

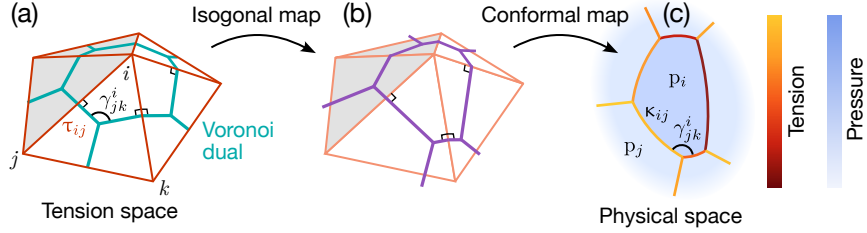


FIG. 8. (a) Non-Euclidean tension triangulation (red) with its Voronoi dual (cyan) constructed from the triangle circumcenters in the plane of each triangle. (The drawing as an embedding in 3D is only for illustration purposes. Only the intrinsic geometry, encoded in the edge lengths τ_{ij} , matters.) (b) Isogonal modes displace the cell vertices in the plane of the respective tension triangle. (b) The conformal map trades Gaussian curvature of the tension triangulation for line curvatures κ_{ij} of cell interfaces. Physically, this implies pressure differences between cells (Young–Laplace law).

tion leaves force balance invariant, this leads to a force-balanced planar cell tessellation. The stress-free, Voronoi reference state now has non-zero curvature, but constant pressure. The Voronoi state is mapped to the physical cell tessellation by the isogonal and conformal mode, both of which preserve the local force balance constraints. The isogonal mode acts first (since isogonal displacement fields exist only for polygonal tessellations with straight edges). The isogonal displacement takes place in the tangent space of the curved tension manifold. This is valid when the isogonal displacement is small compared to the scale $1/\nabla\lambda \sim 1/\sqrt{K}$ of the tension manifold curvature. The conformal mode conformally maps the curved, but constant-pressure isogonal cell tessellation to the physical cell tessellation (flat, but with pressure differentials). This picture, substantiated by the machinery of discrete conformal maps and multiplicatively weighted tessellations, is illustrated in Fig. 8 (see Fig. 16 for a larger tissue patch). Besides giving a simpler geometric meaning to the isogonal potential for non-flat triangulations, the above interpretation is useful for passing to the continuum limit as is explained in App. F.

In summary, incorporating pressure gradients generalizes the results for a flat tension triangulation to the generic case in which the tensions τ_{ij} form a curved, or “buckled,” triangulation. The tension triangulation continues to act as a mechanical reference state, now with non-zero curvature. Hence, in the discrete setting, we recover the same picture as in the continuum theory: a conformal embedding of the tension manifold defines a stress-free reference state for the tissue.

While we have assumed that the cell tessellation lies in a flat plane, Eqs. (44), (48) immediately generalize to tissues on curved surfaces, e.g., the ellipsoidal shape of the early *Drosophila* embryo. In this case, the angle deficit must be computed with respect to the curvature of the target surface. On such curved surfaces, out-of-plane force balance needs to be accounted for in addition to the in-plane force balance $\text{div } \sigma = 0$.

IV. NETWORK TOPOLOGY AND T1 TRANSITIONS

Up to this point, we considered the problem of finding force-balanced states for a given, fixed set of tensions. This corresponds to elastic deformations of the cell tessellation. However, the tissue can also remodel *plastically* by changing the tension triangulation, which acts as a reference state, for instance by smooth changes in the tensions τ_{ij} . Large plastic deformations require topological modifications by neighbor exchange (T1) or cell extrusion (T2) events, which plastically deform the intrinsic tension network by changing its adjacency.

In the previous section, we explained that the tension triangulation defines a piecewise-linear Riemannian manifold. However, different triangulations can realize the same tension manifold. For example, consider different triangulations of the same planar domain (Fig. 9, top), or subdivisions of a given triangulation. Therefore, the triangulation contains additional information/degrees of freedom, namely its adjacency graph (two cells i, j are adjacent if they share an interface in real space). It defines *how* the tension manifold is “tiled” by individual tension triangles, and encodes the local tension configuration. As we will see below, this information is essential for determining when T1s occur.

A. Geometric representation of triangulation topology by circle packs

The (graph) topology of a triangulation is encoded by its adjacency matrix A_{ij} , with $A_{ij} = 1$ if two cells share an edge, and $A_{ij} = 0$ otherwise. (Note that in soft-matter physics convention [12], “topology” refers to the cell adjacency graph, and not the topology of the tension triangulation as a simplicial complex, which we assume to be that of a disk).

The Koebe–Andreev–Thurston circle-packing theorem [37] shows that every triangulation adjacency graph (maximal planar graph) can be represented by a circle packing: a planar drawing with one circle per cell i so

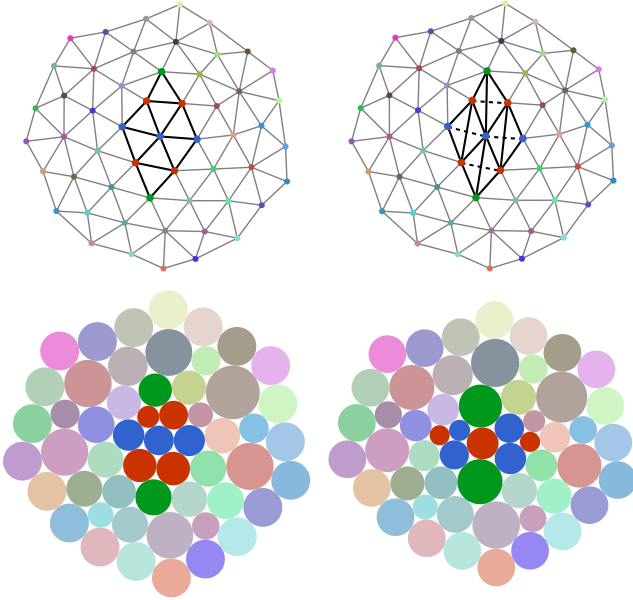


FIG. 9. Two distinct tension triangulations (top) and the circle packs corresponding to their adjacency graph. Both triangulations triangulate the same region of the plane, and thus encode the same tension metric \mathbf{g} and domain Ω . However, their adjacency graphs differ due to T1 transitions in the highlighted region. This difference is reflected in the corresponding circle packings, computed using the uniform neighbor algorithm [37].

that two circles are tangent if and only if the corresponding cells are adjacent (Fig. 9, bottom). With the radii of the boundary circles fixed to unity as in Fig. 9, the circle packing is rigid (i.e., uniquely determined up to global translation and rotation). The packing, thus, yields a unique geometric representation of the adjacency relations. (Alternatively, one can fix the boundary circles to be tangent to the unit disk, which yields a packing unique up to Möbius transformations of the disk [37]; see Fig. 18 in App. G).

Circle packings were introduced by Thurston as discrete approximations of conformal maps. Via this correspondence, we can represent topology in the continuum limit. Indeed, one can reformulate circle packings in terms of the decorated discrete conformal maps introduced in Sect. IIC [21]. Let us think of the adjacency graph as a triangulation which “forgets” the geometric information in the edge lengths τ_{ij} – instead, all edges have the same length. More precisely, we define the adjacency triangulation as a decorated triangulation with edge lengths 1 and vertex circle radii $1/2$ (so the vertex circles are tangent). A discrete conformal embedding with scale factors Λ_i hence results in a circle packing: a pattern of circles in the plane with radii $\Lambda_i/2$ so that two circles i, j are tangent if cells i, j are adjacent. We denote the circle centers by ζ_i . Constructing the tesselation dual to the circle packing makes it clear that cell shapes are

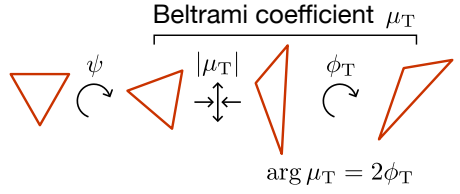


FIG. 10. Map from a reference equilateral triangle to tension triangle defines local tension configuration (LTC). The singular-value decomposition decomposes the map into a rotation, a shear, and a second rotation. The last two operations determine the anisotropy magnitude and orientation, and are combined into the complex-valued Beltrami coefficient $\mu_T = |\mu_T|e^{2i\phi_T}$.

“as circular as possible” in the ζ_i embedding. Each cell has an area $\sim \Lambda_i^2$. The boundary circle radii define the boundary condition for the discrete conformal map.

Just like the tension triangulation defines a surface with Riemannian metric \mathbf{g} , the adjacency triangulation defines a Riemannian “adjacency metric” \mathbf{a} . The “Thurston-embedding” ζ_i is the discrete equivalent of the isothermal coordinates ζ for the adjacency metric \mathbf{a} presented in the companion paper. The natural boundary condition for isothermal coordinates (conformal factor $\Lambda|_{\partial\Omega} = 1$ on the boundary) is the continuum equivalent of $\Lambda_i = 1$ for boundary circles. The Thurston embedding provides a consistent basis to encode the cell density (and hence cell area) as $n(\zeta_i) \propto \Lambda_i^{-2}$. By contrast, the “tension density” (isotropic stress) is reflected in the conformal factor Λ_i^{-1} of the tension triangulation.

Overall, circle packings convert the “combinatorial” information in the adjacency matrix A_{ij} into geometric fields, the embedding ζ_i and the conformal factor Λ_i . This representation may also be useful for analyzing cell tilings extracted from experimental data. Notably, circle packings also admit “fixed” boundary conditions, e.g., such that the boundary circles are tangent to the unit disk. This way, one can align multiple tilings (e.g., from different experiments) to a common domain for analysis. Numerically, circle packs can be efficiently computed using the uniform neighbor algorithm [37].

B. Local tension configuration parameter and Beltrami coefficients

We can also use the adjacency triangulation and the associated circle packing to describe the local tension configuration (LTC). In the tension-triangulation framework, the LTC is defined by the shape of a tension triangle (ijk) in terms of an SVD of an asymmetric rank-two matrix of edge tension vectors [17]. Equivalently, in the present context, we can define the tension triangle shape by the map T that transforms a reference equilateral triangle – the corresponding element of the adjacency metric triangulation – into the given tension triangle. The

LTC thus relates the (discrete) adjacency metric and the tension metric.

T is a linear map since it is defined by its action on two triangle side vectors (alternatively, by its action on vertices and linear interpolation, App. G). It can thus be represented by an asymmetric matrix T_{ab} acting on triangle vertex coordinates in the plane, which can be parametrized via a singular value decomposition $T = R(\phi_T) \cdot \Sigma_T \cdot R(\psi)^T$ (Fig. 10). We previously used this construction to define a set of LTC order parameters (App. G). The first SVD angle ψ , the “LTC phase”, determines if a triangle is acute or obtuse. Acute triangles correspond to “tension cables”, chains of high-tension interfaces. The opposite case (obtuse triangle) has been termed a “tension bridge”, corresponding to an alternating pattern of high- and low tensions [17]. The diagonal matrix $\Sigma_T = \text{diag}(s_1, s_2)$ of singular values and the second angle ϕ_T determine the direction and magnitude of the tension anisotropy. Both are conveniently combined into the complex-valued Beltrami coefficient, normalized to be independent of the triangle area:

$$\mu_T = |\mu_T| e^{2i\phi_T}, \quad (49)$$

with $|\mu_T| = \frac{\sqrt{s_1} - \sqrt{s_2}}{\sqrt{s_1} + \sqrt{s_2}}$. (In Refs. [9, 38] we used the notation $q = |\mu_T|$.)

Let us now connect the LTC parameters of a single triangle to circle packs. Let us denote the vertices of the equilateral reference triangle by $(\zeta_1, \zeta_2, \zeta_3)$, and those of the target tension triangle by (τ_1, τ_2, τ_3) . The linear map T transforms $T \cdot \zeta_\mu = \tau_\mu, \mu = 1, 2, 3$. To make contact with the companion paper, we use complexified notation, where $\zeta = \zeta_1 + i\zeta_2, \bar{\zeta} = \zeta_1 - i\zeta_2$. The matrix T becomes:

$$T(\zeta, \bar{\zeta}) = T \cdot \zeta = \frac{(T_{11} + T_{22}) + i(T_{21} - T_{12})}{2} \zeta \quad (50)$$

$$+ \frac{(T_{11} - T_{22}) + i(T_{21} + T_{12})}{2} \bar{\zeta}$$

Eq. (49) is then equivalent to the standard definition of the Beltrami coefficient in complex analysis [39]:

$$\mu_T = \frac{\partial T / \partial \bar{\zeta}}{\partial T / \partial \zeta} \quad (51)$$

We now upgrade T , defined separately for each triangle, to a globally defined map $T(\zeta, \bar{\zeta})$ from the circle-packing of the adjacency graph to the 2D tension triangulation. At vertices, $T(\zeta_i) = T(\tau_i)$. Elsewhere, $T(\zeta)$ is defined by linear interpolation (App. A), so that on each triangle, the Jacobian $(\nabla T)_{ijk}$ is constant.

The embeddings ζ_i, τ_i of the adjacency and tension triangulation are discrete conformal and therefore (approximately) preserve triangle shapes, and only change their scale (if the triangulations are highly non-planar, there are distortions). Furthermore, the adjacency triangulation is composed of equilateral triangles. Therefore, locally, $T(\zeta, \bar{\zeta})$ maps equilateral triangles to tension triangles. The Jacobian $(\nabla T)_{ijk}$ is thus equivalent to the single-triangle LTC matrix T .

The adjacency triangulation provides an intrinsically defined gauge field (or connection) that relates the orientations of adjacent reference triangles. Locally, the LTC phase ψ measures the triangle’s hexatic phase *relative to the nematic phase* ϕ_T . Spatial correlations in ψ can, therefore, be used to define a “hexanematic” order parameter [9]. For a network with coordination number $z = 6$ for every cell, the adjacency triangulation is a regular lattice of equilateral triangles. Thus, the reference triangles are globally aligned, and the hexatic phase in real space is given by $\phi_T + \psi$. Topological defects (cells with coordination number $\neq 6$) will distort the adjacency triangulation and therefore act as an obstruction to hexatic order in physical space. By contrast, the Beltrami coefficient μ_T is independent of the scale and orientation of the reference triangles.

In the continuum limit, ζ_i and τ_i converge to the isothermal coordinates for the adjacency and tension metrics \mathbf{a}, \mathbf{g} , and $\mu_T = (\partial_\zeta T) / (\partial_\zeta T)$ becomes the Beltrami coefficient “ $\mu_{\zeta|z}$ ” which the companion paper used to define tension anisotropy in the continuum. Representing hexatic order (or its absence) in the adjacency triangulation and the LTC phase ψ in the continuum requires additional order parameters.

The tension anisotropy encoded in μ_T describes how tension τ_{ij} depends on interface orientation. Importantly, it is *distinct* from the macroscopic stress anisotropy, which, by Eq. (17), additionally depends on the interface lengths ℓ_{ij} (a short interface contributes less to the stress). Indeed, we showed that the macroscopic stress is determined by the isogonal mode θ_i and independent of the local tension configuration. Instead, the tension triangulation acts much like a finite-element mesh onto which the isogonal potential is discretized. Microscopic tension and macroscopic stress can be assessed experimentally by laser ablation on different scales (cf. Fig. 1).

C. T1 threshold

When the length of a cell-cell interface vanishes, $\ell_{ij} = 0$, a T1 transition takes place, corresponding to an edge flip in the tension triangulation. The edge lengths ℓ_{ij} are determined by the local geometry of the tension triangulation and isogonal mode (Eq. (13)), and $\ell_{ij} = 0$ corresponds to a *generalized Delaunay criterion*. We now obtain a “T1-threshold” in terms of these quantities.

The T1 yield strain can be calculated from the tension network microstructure. In principle, the length ℓ_{ij} depends on the two tension triangles $(ijk), (ijl)$ meeting at the edge (ij) . However, due to their shared edge, adjacent triangles are strongly correlated [38]. We therefore consider symmetric kites in which the (ijk) and (ijl) are identical so that one is obtained from the other by a π -rotation. One can then directly calculate ℓ_{ij} from the isogonal deformation F^1 and the shape of a tension triangle (ijk) , described by the LTC order param-

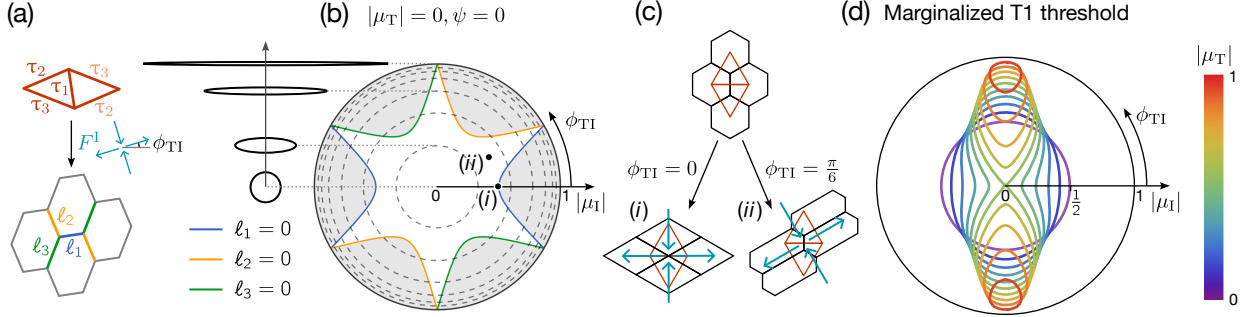


FIG. 11. T1 Threshold for a regular lattice. (a) Geometry setup and labels. The tension triangle is oriented such that the anisotropy axis points along the x -axis (i.e. $\phi_T = 0$). The angle $\phi_{TI} = \phi_I - \phi_T$ measures the isogonal deformation axis relative to this tension anisotropy axis. (b) Locus where one of the edge lengths ℓ_α vanishes in as a function of the isogonal deformation anisotropy $|\mu_I|$ and orientation ϕ_{TI} for an equilateral tension triangle $|\mu_T| = 0$ with (relative) lattice orientation $\psi = 0$. Areas shaded in gray are unphysical configurations where one of the edge lengths would be negative. (c) Illustration of isogonal stretching along an edge (i) and perpendicular to an edge (ii). In the latter case, the T1 threshold approaches $|\mu_I| = 1$ where the deformation becomes degenerate. (d) T1 threshold “marginalized” over the shape phase ψ for a range of magnitudes of tension anisotropy $|\mu_T|$.

eters. Analogously, the isogonal deformation F^I is (up to a scale factor) characterized by its Beltrami coefficient μ_I encoding anisotropy magnitude $|\mu_I|$ and orientation $\arg \mu_I = 2\phi_I$. Using Eq. (19), we compute the three lengths $\ell_{1,2,3}(\mu_T, \mu_I, \psi)$ corresponding to the triangle (Fig. 11a). By rotation invariance, $\ell_{1,2,3}$ only depend on the relative angle $\phi_{TI} = \phi - \phi_T$. A T1 happens whenever one of the lengths hits zero, defining a critical manifold

$$\mathcal{C}_{T1} : \min_i \ell_i(|\mu_I|, |\mu_T|, \phi_{TI}, \psi) = 0 \quad (52)$$

Fig. 11b shows \mathcal{C}_{T1} in the polar $(|\mu_I|, \phi_{TI})$ plane for the case of an equilateral tension triangle ($|\mu_T| = 0$) with phase $\psi = 0$. Additional plots for different triangle shapes ($|\mu_T|, \psi$) are shown in Fig. 19.

The T1 threshold manifold \mathcal{C}_{T1} defines a yield strain magnitude $|\mu_I^{T1}|(|\mu_T|, \phi_{TI}, \psi)$. In the regular lattice, this yield strain sensitively depends on the (hexatic) lattice orientation $\phi_T + \psi$ relative to the principal shear orientation ϕ as illustrated in Fig. 11c [40]. The yield strain is minimal for shear perpendicular to a cell interface Fig. 11c(i), while shear exactly parallel to a cell interface can be indefinitely sustained; Fig. 11c(ii).

T1 transitions can also be triggered in the absence of isogonal deformation by changes in the tensions τ_{ij} , for instance, due to biological dynamics. These can drive one of the cell interfaces to length zero in the stress-free Voronoi reference configuration; see Fig. 19(b). There are, hence, two “classes” of T1 transitions: isogonal “passive” T1s, driven by external forces, and “active” T1s driven by local tension dynamics [17].

The threshold for active T1s depends sensitively on ψ [9, 17]. This is because for a triangle with given anisotropy $|\mu_T|$, the Voronoi edge length sensitively depends on whether the triangle is obtuse ($\psi \approx 0$) or acute ($\psi \approx \pi/6$). This effect is not limited to a regular lattice.

Significant bias in the distribution of ψ is also possible in an amorphous tissue without hexatic order. This is because the hexatic phase in physical space is given by $\psi + \phi_T$, so sufficient disorder in the nematic phase ϕ_T (with a standard deviation around $\pi/6$) is sufficient to destroy hexatic order even if the ψ -distribution is sharply peaked. Capturing this subtle interplay between nematic and hexatic order that is captured by the LTC parameters and their role for T1 transitions (both active and passive) poses an interesting challenge for building continuum theories. It has important applications in understanding the emergence of hexatic order in tissues such as the *Drosophila* pupal wing [41] and eye epithelia [42].

A significant simplification of the T1 threshold can be obtained when ψ is uniformly distributed. One can then define a “marginal” T1 manifold

$$\tilde{\mathcal{C}}_{T1} : \min_{i=1,2,3} \min_{\psi} \ell_i(|\mu_I|, |\mu_T|, \phi_{TI}, \psi) = 0, \quad (53)$$

which tracks when a T1 will first happen for any value of ψ . A family of T1 thresholds in the polar $(|\mu_I|, \phi_{TI})$ plane is shown in Fig. 11(d). For $|\mu_T| = 0$, this marginalized T1 threshold is simply given by $|\mu_I| = 1/2$. The same is true when exchanging I and T. In fact, the entire marginal T1 manifold is symmetric under this exchange; see Fig. 20a. In other words, macroscopic stress anisotropy and microscopic tension anisotropy play identical roles in the ψ -marginalized setting. In fact, one can define a “composite” Beltrami coefficient,

$$\mu_{TI} := \frac{\mu_T + e^{-2i\phi_{TI}}\mu_I}{1 + e^{-2i\phi_{TI}}\bar{\mu}_T\mu_I}, \quad (54)$$

corresponding to the composite mapping $\zeta \mapsto (F^I \cdot T) \cdot \zeta$ where the individual factors have Beltrami coefficients μ_T and μ_I . (μ_{TI} is the discrete per-triangle equivalent of $\mu_{\zeta|w}$ in the companion paper [11].)

The locus $|\mu_{\text{TI}}| = 1/2$ provides a good approximation of \tilde{C}_{T1} ; see Fig. 20(c). The approximation of the T1 threshold through the composite Beltrami coefficient μ_{TI} makes an elegant formulation of plastic flow in the continuum possible [11]. This formulation uses quasiconformal maps to represent tension anisotropy and isogonal strain in the continuum, making μ_{TI} a natural object in the theory.

In summary, using the link between geometry (isogonal mode F^1) and mechanics (stress tensor σ), one can calculate the yield stress of a “generalized foam” with arbitrary tension configurations from the microscopic geometry. Yielding occurs via T1 transitions, which reduce the isogonal strain. Related questions have been previously studied in the literature on 2D foams [43, 44] via phenomenological approaches.

DISCUSSION

Unlike conventional elastic materials, many living tissues have no fixed reference state and control active stresses via motor molecule activity, rather than a constitutive relationship. By studying the geometry of force balance, we showed that the configuration of active tensions in 2D epithelia, interpreted as a triangulation dual to the cell tessellation, gives rise to an emergent, force-balanced reference state where tensions balance against a uniform pressure. This explains how cells can control a tissue’s shape through the microscopic stress configuration.

Emergent elasticity, soft modes, and stress transformation laws

Our coarse-graining analysis confirms all elements of the top-down, continuum theory presented in the companion paper and clarifies their microscopic origin (see Table I). Overall, we find that the mechanics of ATNs can be described as “emergent elasticity”: the combination of active tensions and pressure allows tissues to resist external (shear) forces, in contrast to models where the tissue shear modulus can be tuned to vanish [13, 14]. Tissue flow emerges through the adiabatic dynamics of active tensions, “locked in” by topological cell rearrangement.

Deformations from the reference to the physical configuration are characterized by two soft modes, conformal and isogonal modes. Together, they exhaust the space of deformations compatible with the constraints of force balance. These modes act as mediators between the “microscopic” and macroscopic mechanical state of the tissue. Put concisely, a stress-strain relationship (or stress transformation law) emerges from how the active force dipoles (cell edges) are embedded into physical space.

The isogonal mode sets the lengths of cell-cell interfaces and determines the macroscopic stress tensor. By contrast, the conformal mode sets cell edge orientation,

so that force balance in the conformal sector can be thought of as *torque balance*. Via the Young–Laplace law, the conformal mode parametrizes the gradients of intracellular pressure.

These results extend observations from literature on foam mechanics [45–47], which noted the invariance of force balance under Möbius transformations of a 2D foam, and demonstrated it in beautiful experiments [48]. Here, we generalized from an ordinary foam with fixed surface tensions to an arbitrary tension triangulation, and from a global to a local (triangle-wise) Möbius symmetry, which approximates arbitrary conformal maps in the continuum limit. Finally, by studying the interaction between the isogonal and conformal modes, we showed how the conformal factor (geometry) is connected to pressure (mechanics).

Discrete–continuum correspondence

The key to linking microscopic and macroscopic scales lies in formulating mechanics in geometric terms. This allowed us to draw on the powerful mathematics of discrete conformal maps, which goes back to the work of Thurston and Koebe on circle packings. We showed that multiplicatively weighted Voronoi and power tessellations, previously introduced to parametrize mechanically balanced cell tessellations [8, 31], can be understood as the image of the tension triangulation under discrete conformal maps. This finding, a “dual” formulation of discrete conformal maps, may be of independent mathematical interest. The peculiar algebra of multiplicatively weighted tessellations results from a conformal symmetry. Curvature of the tension triangulation acts as a source of conformal deformation, and thereby pressure gradients, leading to a geometric, generalized version of the von Neumann law for the pressure in a foam bubble. In the continuum limit, these maps converge to a conformal embedding of a smooth tension manifold, substantiating the picture described in the companion paper. Table I provides a summary of the “discrete–continuous dictionary”.

The formalism of discrete conformal maps underlies powerful numerical algorithms for surface processing, developed by the computer graphics community. These algorithms can now be harnessed for numerical simulations of tissue mechanics. In particular, there has been recent interest in simulations compatible with automatic differentiation. Such codes can use machine-learning technology to explore the model “phase space” and identify cell-level dynamics capable of generating a target shape [49]. A major difficulty lies in incorporating discrete, non-differentiable events like cell division and rearrangement. The close link between discrete conformal geometry and its smooth counterpart may inspire new approaches to tackle this challenge.

The discrete–continuum correspondence is also closely linked to the finite-element method. The barycentric interpolation method we use to pass between the cell- and

continuum level functions is known as the linear Lagrange element in the finite-element literature [19]. The discrete Laplace operator Eq. (46) also arises in finite-element discretizations. Strikingly, in this interpolation scheme, the discretization of a continuous stress tensor reproduces the microscopic force-balance equations (App. C2) [27].

Cell adjacency, local tension configuration, and topological remodeling

The mechanical state of an ATN is controlled by its tension triangulation τ_{ij} . This triangulation encodes two distinct pieces of information: first, the (piecewise-linear) surface it defines, and second, the adjacency graph of the cell network. Different triangulations can realize the same surface (as in, for example, different triangulations of the plane).

Our results show that the macroscopic mechanics is determined by the tension surface alone, independently of how it is triangulated. The macroscopic stress tensor is determined by the isogonal potential $\theta(\tau)$. Different triangulations only change the “interpolation nodes” τ_i at which $\theta_i = \theta(\tau_i)$ is evaluated. Coarse-graining, hence, leads to a significant simplification; the cell-level triangulation appears as a finite-element-like discretization of the continuum theory. In the latter, the tension surface is encoded by the Riemannian tension metric g .

The adjacency graph instead corresponds to the “adjacency metric” a of the continuum theory. This graph is conveniently parametrized by its “Thurston coordinates” ζ_i , the centers of the corresponding circle packing. The Thurston coordinates translate topology into geometry and may be a useful tool to analyze the adjacency patterns and dynamics of tissues in experimental data [50]. For such data analysis, circle packs to the unit disks may be convenient, which automatically register different datasets into a common reference frame.

To accommodate large, plastic deformations, cells in an active tension network can rearrange, dynamically changing the adjacency graph. These inherent plastic effects differentiate ATNs from generic elasticity materials and are an immediate consequence of the underlying discrete structure. Here, the triangulation “microstructure” becomes relevant [38]. We determined the threshold beyond which internally and externally driven deformations trigger yielding through cell rearrangements (T1 transitions) as a function of local order parameters furnished by force-balance geometry.

T1 transitions

We described the shape of individual tension triangles via the local tension configuration (LTC) parameters. The LTC parameters and the isogonal strain determine an effective yield strain beyond which internal tension anisotropy or from isogonal strain stress triggers

T1s. These occur whenever a cell-cell interface reaches zero length, $\ell_{ij} = 0$. We showed that the T1 threshold is *local*: it depends on the configuration at interface ij only, in contrast to the energy barriers for T1 transition in “elastic” vertex models, like the area-perimeter model. The exact, geometric T1 threshold is well approximated by the combined Beltrami coefficient of tension and isogonal anisotropy. This justifies the phenomenological ansatz for the T1 rate made in the continuum theory. A rigorous link between the tissue’s mechanical state and local plasticity is a key advance of the geometric framework we propose.

In an active tension net, the T1 threshold sets a limit on the magnitude of the isogonal deformation and hence bulk stress. Beyond the isogonal “yield strain”, cell interfaces collapse, which leads to T1s that relax the isogonal deformation. Such a yield *strain* is unusual: in conventional elasticity, the onset of plastic deformation is governed by a yield stress instead. However, in an ATN, the yield strain is determined purely geometrically and independent of the strength of the microscopic bonds, i.e. the effective stiffness p_0 .

This limit also has an interesting mechanical interpretation linked to granular materials. Mechanically, the constraint $\ell_{ij} \geq 0$ means that the physical stress is purely contractile (for $\ell_{ij} < 0$, an interface would exert a pushing force). A negative definite stress corresponds to a convex Airy function. We showed that the Airy function for tensile stress is given by the (Legendre dual of the) isogonal potential θ . T1s dynamically maintain the convexity of θ [51]. Lack of convexity leads to a mechanical instability, which is “resolved” by an edge flip in the triangulation.

Tension networks and granular materials

The mechanical Legendre duality discussed in Sect. IC connects tension networks to (frictionless) granular materials. For instance, the isogonal mode of an ATN corresponds to the wheel moves between the different stress states of a granular material. The T1 threshold also applies to granular materials, where T1s correspond to the loss of contact between two grains as the pushing force they exert on one another vanishes. Thus, the “T1 threshold” in the granular setting bounds the admissible stress states compatible with a given contact network.

We demonstrated that ATNs exhibit a form of “emergent elasticity”. There has also been recent interest in the emergent elastic behavior in granular materials [52]. Appealing to an analogy with (tensor) electromagnetism [53], Ref. [52] postulates that the stress tensor σ_{ab} and the momentum density obey a generalized version of Maxwell’s equations. Ref. [52] emphasizes that this is a phenomenological hypothesis, since the equivalent of Ampere’s law has no clear mechanical origin. In the static limit, this assumption entails that $\epsilon_{ab}\partial_b\epsilon_{cd}\partial_d\sigma_{ac} = 0$; i.e., the stress is integrable and de-

Discrete	Continuum
Tension triangulation	Riemann surface with tension metric
Mult. weighted Voronoi tesselation	Isothermal embedding of tension metric
Power tesselation	Isogonal/curl-free mode
Piecewise Möbius transformation	Conformal mode
Adjacency graph and circle packing	Adjacency metric and its isothermal embedding
Local tension configuration	Quasi-conformal map from adjacency- to tension-embedding
Generalized Delaunay criterion (T1 threshold)	Relaxational dynamics for adjacency metric

TABLE I. Dictionary for the discrete/continuum correspondence.

ries from a vector field φ_a . Ref. [52] further assumes “linear dielectric” behavior, i.e., a linear stress-strain relationship between σ_{ab} and φ_a . These two hypotheses mean treating a granular system as an effectively elastic medium, which is in good agreement with numerical simulations (once the elastic moduli are fitted to the data).

By contrast, the present manuscript and the companion paper derive the emergent elastic behavior from the microscopic force balance constraints. The effective Airy potential θ has a direct microscopic interpretation (the isogonal mode), and one can compute the effective elastic moduli in terms of the microscopic model. The stress is not, in general, integrable, due to the curvature of the tension triangulation. Indeed, in the companion paper, we showed that $\epsilon_{ab}\partial_b\epsilon_{cd}\partial_d\sigma_{ac} = \Delta^2\theta = 0$ only when the cell and tension “densities” are proportional across the tissue.

It is an interesting question whether the geometric formalisms for ATNs presented could also be used to derive the macroscopic behavior of granular materials.

Mean-field dynamics of tension networks

We described how active tensions τ_{ij} determine cell positions \mathbf{r}_{ijk} . To describe biophysical dynamics, this mechanical formalism must be combined with a concrete model for tension dynamics (e.g., stochastic fluctuations [10], control by morphogens, or mechanical feedback loops [9]). Such microscopic models can be coarse-grained using the LTC parameters employed in our analysis of T1 transitions. Ref. [38] proposed characterizing the mechanical state of a tissue patch by the local distribution \mathcal{P} of tension triangle shapes in a mesoscopic tissue patch. Hydrodynamic variables are given by the moments of this distribution, e.g., the anisotropy tensor $Q = \mathbb{E}_{\mathcal{P}}[\mu_T]$. In the mean-field approximation, tension dynamics $\partial_t\tau_{ij} = \dots$ on the cell-level lead to a Fokker-Planck equation for \mathcal{P} , and, after averaging, the dynamics of the hydrodynamic variables. The mean-field framework also allows incorporating the LTC phase ψ , which has important effects on T1-transitions. In Ref. [17], where we analyzed experimental data from *Drosophila*

convergent extension, we argued that a certain “polarization” in ψ is important to facilitate T1s. In the present work, for simplicity, we marginalized over ψ . Together, the present mechanical formalism (statics), and the mean-field approach of Ref. [38] (dynamics) form a consistent framework to coarse-grain cell-level into continuum models for morphogenetic tissue dynamics.

Control of intracellular pressure

We showed that in mechanical balance, cells cannot change their pressure and tensions independently. A generic change in the tensions τ_{ij} leads to a non-zero angle deficit δ_i (discrete curvature), similar to models of plant leaf wrinkling due to non-uniform growth. By Eq. (48), tension curvature leads to pressure differentials.

Over longer timescales, cells actively regulate their volume and osmotic pressure, e.g., via ion pumping. The above suggests that this pressure regulation may be coupled to the tension in the actomyosin cytoskeleton. For example, cells could reduce pressure gradients by modulating their overall tension level

$$\frac{\partial_t \tau_{ij}}{\tau_{ij}} = -\beta [(\Delta \log p)_i + (\Delta \log p)_j] \quad (55)$$

Eq. (55) is a discrete Ricci flow [54] which smoothes out curvature in the tension manifold [55]. It is also interesting to note that the pressures p_i are fully determined by their values at the tissue boundary, which may enable local sensing of large-scale deformations.

Outlook

Our geometric continuum formulation prepares the ground for systematic coarse-graining of cell-level dynamics, which takes the form of plastic remodeling of the tension network. We believe that the study of active plastic flow gives rise to several interesting directions for future research.

Large plastic deformations require topological T1 transitions, which, in a hexagonal lattice, create “topological

defects” (pairs of 5- and 7-sided cells). It will be interesting to study the effect of these defects in more detail. Classically, lattice defects are quantified by a Burgers vector. How are Burgers vectors linked to the Thurston packing, and geometric approaches that use torsion (a concept from differential geometry) to measure lattice defects [56]? Interestingly, the concept of torsion can be naturally translated into the discrete setting [57].

Continuing on the theme of differential geometry, discrete conformal maps are deeply linked to hyperbolic geometry [21, 58]. Indeed, hyperbolic geometry can be used to characterize (a special case of) multiplicative weighted tessellations [59] by viewing the (complex) plane of the tessellations as the boundary of three-dimensional hyperbolic space. This duality, much studied in high-energy physics, may open up a new perspective on the mechanics of the cell tessellations.

Beyond biological tissues, our work has several connections to the literature on foam mechanics; indeed, the active tension network model can be thought of as a generalized foam. By elucidating the role of tension triangulation curvature and the isogonal mode, we unify

and extend previous work. Additionally, the mechanical Legendre duality we describe highlights close connections between tension networks and granular materials. This connection may merit further study.

Going forward, it will be interesting to consider other examples of active solids whose shape is determined by the requirement to balance an intrinsic, active stress. Our work shows that it is key to understand how the microscopic structure determines the transformation of active stress under deformations. Systematic study of such “stress transformation laws” may uncover rich geometry and exotic mechanical phases.

ACKNOWLEDGMENTS

B.I.S. acknowledges support of the NSF Physics (PoLS) grant #2210612. N.H.C. is supported by a PCTS fellowship. F.B. acknowledges support by the Gordon and Betty Moore Foundation post-doctoral fellowship (grant #2919).

[1] M. C. Marchetti, J. F. Joanny, S. Ramaswamy, T. B. Liverpool, J. Prost, M. Rao, and R. A. Simha, Hydrodynamics of soft active matter, *Reviews of Modern Physics* **85**, 1143 (2013).

[2] C.-P. Heisenberg and Y. Bellaïche, Forces in Tissue Morphogenesis and Patterning, *Cell* **153**, 948 (2013).

[3] S. F. Gilbert and M. J. F. Barresi, *Developmental Biology* (Sinauer Associates, Sunderland, Massachusetts, 2016).

[4] S. Alt, P. Ganguly, and G. Salbreux, Vertex models: From cell mechanics to tissue morphogenesis, *Philosophical Transactions of the Royal Society B: Biological Sciences* **372**, 20150520 (2017).

[5] R. Sknepnek, I. Djafer-Cherif, M. Chuai, C. Weijer, and S. Henkes, Generating active T1 transitions through mechanochemical feedback, *eLife* **12**, e79862 (2023).

[6] K. Bambadekar, R. Clément, O. Blanc, C. Chardès, and P.-F. Lenne, Direct laser manipulation reveals the mechanics of cell contacts in vivo, *Proceedings of the National Academy of Sciences* **112**, 1416 (2015).

[7] N. Noll, S. J. Streichan, and B. I. Shraiman, Variational Method for Image-Based Inference of Internal Stress in Epithelial Tissues, *Physical Review X* **10**, 011072 (2020).

[8] N. Noll, M. Mani, I. Heemskerk, S. J. Streichan, and B. I. Shraiman, Active tension network model suggests an exotic mechanical state realized in epithelial tissues, *Nature Physics* **13**, 1221 (2017).

[9] N. H. Claussen, F. Brauns, and B. I. Shraiman, A geometric-tension-dynamics model of epithelial convergent extension, *Proceedings of the National Academy of Sciences* **121**, e2321928121 (2024).

[10] S. Kim, M. Pochitaloff, G. A. Stooke-Vaughan, and O. Campàs, Embryonic tissues as active foams, *Nature Physics* **17**, 859 (2021).

[11] N. H. Claussen, F. Brauns, and B. I. Shraiman, Elasticity without a reference state: Continuum mechanics of active tension nets, arXiv 10.48550/arXiv.2601.08968 (2026).

[12] D. L. Weaire, D. L. Weaire, and S. Hutzler, *The Physics of Foams*, reprinted ed. (Clarendon Press, Oxford, 2005).

[13] R. Farhadifar, J.-C. Röper, B. Aigouy, S. Eaton, and F. Jülicher, The Influence of Cell Mechanics, Cell-Cell Interactions, and Proliferation on Epithelial Packing, *Current Biology* **17**, 2095 (2007).

[14] D. Bi, J. H. Lopez, J. M. Schwarz, and M. L. Manning, A density-independent rigidity transition in biological tissues, *Nature Physics* **11**, 1074 (2015).

[15] B. Springborn, P. Schröder, and U. Pinkall, Conformal equivalence of triangle meshes, *ACM Transactions on Graphics* **27**, 1 (2008).

[16] Making them orthogonal, rather than, for instance, parallel, is simply a convention that emphasizes the geometric duality of tension triangulation and cell tessellation.

[17] F. Brauns, N. H. Claussen, E. F. Wieschaus, and B. I. Shraiman, The Geometric Basis of Epithelial Convergent Extension, *eLife* **10**.7554/eLife.95521.1 (2024).

[18] F. De Goes, P. Memari, P. Mullen, and M. Desbrun, Weighted Triangulations for Geometry Processing, *ACM Transactions on Graphics* **33**, 1 (2014).

[19] K. Crane, *Discrete Differential Geometry: An Applied Introduction* (2025).

[20] F. Aurenhammer, Power Diagrams: Properties, Algorithms and Applications, *SIAM Journal on Computing* **16**, 78 (1987).

[21] A. I. Bobenko and C. O. R. Lutz, Decorated Discrete Conformal Maps and Convex Polyhedral Cusps, *International Mathematics Research Notices* **2024**, 9505 (2024).

[22] G. K. Batchelor and J. T. Green, The determination of the bulk stress in a suspension of spherical particles to order c^2 , *Journal of Fluid Mechanics* **56**, 401 (1972).

[23] J. H. Irving and J. G. Kirkwood, The Statistical Mechanical Theory of Transport Processes. IV. The Equations

of Hydrodynamics, *The Journal of Chemical Physics* **18**, 817 (1950).

[24] C. Davini, A Continuum Model for Fluid Foams, *Journal of Elasticity* **101**, 77 (2010).

[25] S. Alexander, Amorphous solids: Their structure, lattice dynamics and elasticity, *Physics Reports* **296**, 65 (1998).

[26] J. C. Maxwell, On reciprocal figures and diagrams of forces, *The London, Edinburgh, and Dublin Philosophical Magazine and Journal of Science* **27**, 250 (1864).

[27] M. Desbrun, R. D. Donaldson, and H. Owhadi, Modeling Across Scales: Discrete Geometric Structures in Homogenization and Inverse Homogenization, in *Multiscale Analysis and Nonlinear Dynamics*, edited by M. M. Z. Pesenson (Wiley, 2013) 1st ed., pp. 19–64.

[28] F. De Goes, P. Alliez, H. Owhadi, and M. Desbrun, On the equilibrium of simplicial masonry structures, *ACM Transactions on Graphics* **32**, 1 (2013).

[29] D. Bi, S. Henkes, K. E. Daniels, and B. Chakraborty, The Statistical Physics of Athermal Materials, *Annual Review of Condensed Matter Physics* **6**, 63 (2015).

[30] The Voronoi cells exactly tile the triangulation and are hence a well-defined “unit cell” for computing the dual Batchelor stress.

[31] C. Moukarzel, Geometrical consequences of foam equilibrium, *Physical Review E* **55**, 6866 (1997).

[32] K. Crane, Conformal geometry of simplicial surfaces, in *An Excursion Through Discrete Differential Geometry*, Proceedings of Symposia in Applied Mathematics, Vol. 76 (2020).

[33] P. F. Ash and E. D. Bolker, Generalized Dirichlet tessellations, *Geometriae Dedicata* **20**, 209 (1986).

[34] Note that the centers of the mapped circles are not the images of the original centers, i.e. $\tau_i^{\text{PC}} \neq M(\tau_i)$.

[35] The deviations from circle preservation (and thus exact force balance) are measured by the higher-order Schwarzian derivative $f'''/f' - \frac{3}{2}(f''/f')^2$, they become small if f is slowly varying compared to the cell scale.

[36] J. M. Lee, *Introduction to Smooth Manifolds*, Graduate Texts in Mathematics, Vol. 218 (Springer New York, New York, NY, 2012).

[37] K. Stephenson, *Introduction to Circle Packing: The Theory of Discrete Analytic Functions* (Cambridge University Press, Cambridge, 2005).

[38] N. H. Claussen and F. Brauns, Mean-Field Model for Active Plastic Flow of Epithelial Tissue, *PRX Life* **3**, 023002 (2025).

[39] L. Ahlfors, *Lectures on Quasiconformal Mappings* (D. van Nostrand Company, Princeton, NJ, 1966).

[40] We define the phase $\arg \mu_T$ as $2\phi_T$, not vice versa. This is important in the case $|\mu_T| = 0$ where $\arg \mu_T$ is a priori indeterminate but $\phi_T + \psi$ determines the hexatic phase, so ϕ_T is defined even if tension is isotropic.

[41] A.-K. Classen, K. I. Anderson, E. Marois, and S. Eaton, Hexagonal Packing of Drosophila Wing Epithelial Cells by the Planar Cell Polarity Pathway, *Developmental Cell* **9**, 805 (2005).

[42] L. Couturier, J. Luna-Escalante, K. Mazouni, C. Mestdagh, M.-S. Phan, J.-Y. Tinevez, F. Schweigert, and F. Corson, Pulsatile dynamics propagate crystalline order in the developing Drosophila eye, *Developmental Cell* **S1534580725006379** (2025).

[43] P. Marmottant, C. Raufaste, and F. Graner, Discrete rearranging disordered patterns, part II: 2D plasticity, elasticity and flow of a foam, *The European Physical Journal E* **25**, 371 (2008).

[44] C. Raufaste, S. J. Cox, P. Marmottant, and F. Graner, Discrete rearranging disordered patterns: Prediction of elastic and plastic behavior, and application to two-dimensional foams, *Physical Review E* **81**, 031404 (2010).

[45] D. Weaire, The equilibrium structure of soap froths: Inversion and decoration, *Philosophical Magazine Letters* **79**, 491 (1999).

[46] W. Drenckhan, D. Weaire, and S. J. Cox, The demonstration of conformal maps with two-dimensional foams, *European Journal of Physics* **25**, 429 (2004).

[47] M. Mancini, *Structure and Evolution of Soap-like Foams*, Ph.D. thesis, Universite de Cergy Pontoise (2005).

[48] F. Elias, J.-C. Bacri, F. H. De Mougins, and T. Spengler, Two-dimensional ferrofluid foam in an external force field: Gravity arches and topological defects, *Philosophical Magazine Letters* **79**, 389 (1999).

[49] R. Deshpande, F. Mottes, A.-D. Vlad, M. P. Brenner, and A. Dal Co, Engineering morphogenesis of cell clusters with differentiable programming, *Nature Computational Science* **5**, 875 (2025).

[50] M. Merkel, R. Etournay, M. Popović, G. Salbreux, S. Eaton, and F. Jülicher, Triangles bridge the scales: Quantifying cellular contributions to tissue deformation, *Physical Review E* **95**, 032401 (2017).

[51] Indeed, Eq. (13) shows that the ℓ_{ij} are determined by the 2nd derivative of θ_i , so $\ell_{ij} > 0$ ensures convexity.

[52] J. N. Nampoothiri, M. D’Eon, K. Ramola, B. Chakraborty, and S. Bhattacharjee, Tensor electromagnetism and emergent elasticity in jammed solids, *Physical Review E* **106**, 065004 (2022).

[53] A. Gromov and L. Radzhivsky, Colloquium: Fracton matter, *Reviews of Modern Physics* **96**, 011001 (2024).

[54] T. Tao, Ricci flow, in *The Princeton Companion to Mathematics* (Princeton University Press, Princeton, NJ, 2008) pp. 279–281.

[55] Eq. (55) presents a feedback mechanism for the establishment of force-balance-compatible tensions that operates quasi-statically and requires a non-zero bulk modulus to build up pressure gradients. By contrast, in a compressible tissue, tension incompatibility causes secular elongation or contraction of cell-cell interfaces, requiring different stabilizing mechanisms [8].

[56] A. Yavari and A. Goriely, Riemann–Cartan Geometry of Nonlinear Dislocation Mechanics, *Archive for Rational Mechanics and Analysis* **205**, 59 (2012).

[57] T. Braune, M. Gillespie, Y. Tong, and M. Desbrun, Discrete Torsion of Connection Forms on Simplicial Meshes, *ACM Transactions on Graphics* **44**, 1 (2025).

[58] A. I. Bobenko, U. Pinkall, and B. A. Springborn, Discrete conformal maps and ideal hyperbolic polyhedra, *Geometry & Topology* **19**, 2155 (2015).

[59] D. Eppstein, A Möbius-Invariant Power Diagram and Its Applications to Soap Bubbles and Planar Lombardi Drawing, *Discrete & Computational Geometry* **52**, 515 (2014).

Appendix A: Linear interpolation on triangulations

To translate between discrete and continuous spaces, we define piecewise affine “hat” basis functions $\phi_i(\tau)$ in triangulation space. The ϕ_i are defined by their values

Symbol	Description
i, j, \dots	Cell indices
a, b, \dots	Coordinate indices
\mathbf{n}	Unit normal vector
$\epsilon_{ab}, (\cdot)^\perp$	Rotation by $\pi/2$
τ_{ij}	Interfacial tension
τ_i	2D tension vertex
$\tilde{\gamma}_{ij}^k$	Tension triangulation angle
\tilde{a}_{ijk}	Triangle area
$\tilde{\cdot}$	Triangulation quantity
$\phi_i(\tau)$	Piecewise-linear interpolation
$(\nabla h)_{ijk}$	Discrete gradient of a function
p_i	Intracellular pressures
p_0	Reference pressures (set to $p_0 = 1$)
ℓ_{ij}	Cell edge lengths
a_i	Cell area
ℓ_{ij}	Cell edge lengths
γ_{ij}^k	Tricellular vertex angle
\mathbf{r}_{ij}^k	Tricellular vertex position
\mathbf{r}_{ijk}^V	Voronoi vertex positions
C_i^V	Voronoi tessellation cell
θ_i	Isogonal potential
\mathbf{r}_{ijk}^I	Isogonal vertex positions
C_i^P	Power tessellation cell
$\theta(\tau)$	Continuous isogonal potential
θ^*	Legendre dual potential
F_{ab}^I	Isogonal deformation tensor
σ_{ab}	Tensile stress tensor
$\tilde{\sigma}_{ab}$	Dual stress tensor
$\sigma_{ab}^{\text{tot}} = \sigma_{ab} - p\delta_{ab}$	Total stress tensor
κ_{ij}	Line curvature
$z = x + iy$	Complexified coordinate
$f(z)$	Conformal map
$(\cdot)^C$	Conformally deformed quantity
F_{ab}^C	Conformal Jacobian
$M(z)$	Moebius transformation
λ_i	Discrete conformal factor
C_i^C	Mult. weighted Voronoi tessellation
C_i^{PC}	Mult. weighted power tessellation
δ_i	Angle defect
\mathbf{g}	Tension metric
\mathbf{a}	Adjacency metric
ξ	Lagrangian cell-label coordinates
K	Gaussian curvature
ζ_i, Λ_i	Circle packing centers and radii
T	Map to reference triangle
ψ	LTC phase
μ_T, μ_I	Beltrami coefficients
\mathcal{C}_{T1}	T1-threshold

TABLE II. Overview of notation.

at vertices, $\phi_i(\tau_j) = \delta_{ij}$, and linear interpolation in between. Note that $\phi_i(\tau) = 0$ for τ outside the convex hull of the vertices neighboring i . Crucially, for linear interpolation on a mesh, the mesh faces must be triangular.

It is difficult to define a set of basis functions at the dual vertices \mathbf{r}_{ijk} , and the existence of a convenient interpolation scheme is one of the advantages of working with the triangulation.

We will need expressions for the linear-hat functions and their gradients (see Ref. [19]). Using barycentric coordinates $\zeta_i, \zeta_j, \zeta_k$ for triangle (ijk) , we have $\phi_i(\tau) = \zeta_i(\tau)$. Barycentric coordinates are defined by

$$\zeta = \mathcal{T}^{-1} \cdot (\tau - \tau_k), \quad \mathcal{T} = (\tau_i - \tau_k, \tau_j - \tau_k). \quad (\text{A1})$$

In each triangle (ijk) , the gradient is constant and can be expressed in terms of the basis functions as

$$\nabla \phi_i = \frac{1}{2\tilde{a}_{ijk}} (\tau_k - \tau_j)^\perp \quad (\text{A2})$$

where $\tilde{a}_{ijk} = \frac{1}{2} \det \mathcal{T}$ is the area of triangle (ijk) . These finite element gradients fulfill the relations

$$\nabla \phi_i \cdot (\tau_j - \tau_i) = 1 \quad (\text{A3a})$$

$$\nabla \phi_i \cdot \nabla \phi_j = \frac{1}{2\tilde{a}_{ijk}} \cot \tilde{\gamma}_{ij}^k \quad i \neq j \quad (\text{A3b})$$

$$|\nabla \phi_i|^2 = \frac{1}{2\tilde{a}_{ijk}} (\cot \tilde{\gamma}_{ik}^j + \cot \tilde{\gamma}_{ij}^k) \quad (\text{A3c})$$

These basis functions, equivalent to linear Lagrange elements in finite-element-method terminology, enable linear interpolation and the discretization of differential operators. Given values of a scalar function on triangular vertices h_i , one can linearly interpolate $h(\tau) = \sum_i h_i \phi_i(\tau)$. The gradient is piecewise constant on each triangle (ijk)

$$(\nabla h)_{ijk} = \sum_{l \in \{i,j,k\}} h_l \nabla \phi_l \quad (\text{A4})$$

1. Discrete Laplacian

While the second derivative of $h(\tau)$ is not defined, one can compute the Laplace operator in the weak form

$$\int \phi_i \Delta h d\tau^2 = - \int \nabla \phi_i \cdot \nabla h d\tau^2 \quad (\text{A5a})$$

$$= - \sum_{j, k \sim i} \tilde{a}_{ijk} \nabla \phi_i \sum_{l \in \{i,j,k\}} h_l \nabla \phi_l \quad (\text{A5b})$$

$$= \frac{1}{2} \sum_{j \sim i} (\cot \tilde{\gamma}_{ij}^k + \cot \tilde{\gamma}_{ij}^l) (h_j - h_i) \quad (\text{A5c})$$

where we have made use of the relations Eq. (A3) and $\tilde{\gamma}_{ij}^k$ and $\tilde{\gamma}_{ij}^l$ are the angles opposite edge (ij) . The resulting discretization is referred to as the cotangent-Laplacian:

$$(\Delta h)_i = \frac{1}{2} \sum_{j \sim i} (\cot \tilde{\gamma}_{ij}^k + \cot \tilde{\gamma}_{ij}^l) (h_j - h_i). \quad (\text{A6})$$

Note that $(\Delta h)_i$ represents the Laplacian *integrated* over cell i ; to approximate the continuum Laplace operator, one must additionally normalize by the cell area, $\Delta h(\tau_i) \approx (\Delta h)_i / a_i$.

Strikingly, the weights of the discrete Laplacian are defined by the Voronoi-edge lengths, $(\cot \tilde{\gamma}_{ij}^k + \cot \tilde{\gamma}_{ij}^l) = \ell_{ij}^V / \tau_{ij}$. This can be understood as a result of the divergence formula, integrated over a cell i :

$$a_i(\Delta h)_i = \int_i (\Delta h) da = \int_i \operatorname{div}(\nabla h) da \quad (\text{A7a})$$

$$= \int_{\partial i} \nabla h \cdot d\mathbf{n} \approx \sum_j \ell_{ij} \frac{h_i - h_j}{\tau_{ij}} \quad (\text{A7b})$$

2. Isogonally weighted Laplacian

The definition Eq. (46) also makes sense for non-Voronoi, isogonal tessellations, replacing the Voronoi edge lengths ℓ_{ij}^V by the isogonally deformed ones ℓ_{ij}^I . This weighted Laplace operator depends on the isogonal mode, and reproduces the cotangent Laplacian for $\theta_i = 0$ [18]. In the continuum limit, Eq. (46) corresponds to an anisotropic Laplacian:

$$\Delta h = \frac{1}{\det F^I} \nabla_{\tau} \cdot (\det F^I (F^I)^{-1} \cdot \nabla_{\tau} h) \quad (\text{A8})$$

We verified Eq. (A8) numerically for a periodic lattice. Further, it can be rationalized as follows. For $F^I = \mathbb{I}$, Eq. (46) corresponds to the conventional Laplacian. Applying an isogonal deformation stretches interfaces ℓ_{ij} and changes each $d\mathbf{n}_{ij}$ term in (46) by $(F^I)^{\perp} = (F^I)^{-1} \det F^I$, whereas the area a_i changes by $\det F^I$.

Appendix B: Voronoi and power tessellations

1. Power distance and isogonal gradient

To see the equivalence of the power-distance and gradient-based formulations for the isogonal cell tiling, consider the following transformation of Eq. (14):

$$\tau_i \mapsto \tau_i + \mathbf{c}, \quad \theta_i \mapsto \theta_i - 2\mathbf{c} \cdot \tau_i - c^2 \quad (\text{B1})$$

where \mathbf{c} is an arbitrary constant vector. Then

$$(|\tau_i - \mathbf{r}|^2 + \theta_i) \mapsto (|\tau_i - \mathbf{r}|^2 + \theta_i) - 2\mathbf{c} \cdot \mathbf{r}$$

and therefore, the equation $|\mathbf{r} - \tau_i|^2 - \theta_i \stackrel{!}{=} |\mathbf{r} - \tau_j|^2 - \theta_j$ for the positions of the cell-cell interfaces is invariant. Hence, a linear gradient in θ_i leads to a uniform displacement of tricellular vertices, precisely as in the gradient-based formulation.

Appendix C: Macroscopic stress and isogonal mode

1. Batchelor stress on a periodic lattice

Consider a periodic lattice, shown in Fig. 12, composed of identical tension triangles with edges τ_{μ} , $\mu = 1, 2, 3$,

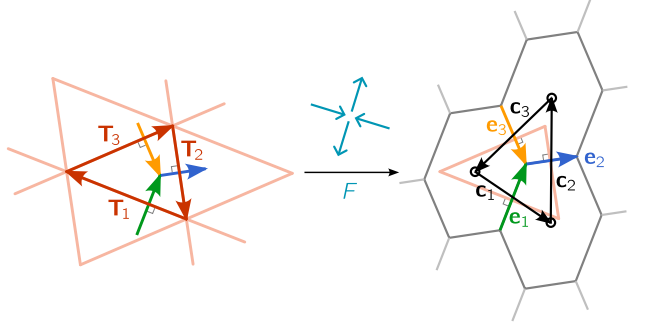


FIG. 12. Geometry and notation for the regular lattice formed from a single tension triangle and the corresponding regular cell tessellation resulting from a uniform isogonal deformation F .

and cell edge vectors $\mathbf{r}_{\mu} = \ell_{\mu} \tau_{\mu}^{\perp} / \tau_{\alpha}$. (Note that we use the index μ to distinguish these triangle edge vectors from the triangulation vertex positions, which are labeled with indices i, j, k .) The displacement vectors between cell centroids are given by $\mathbf{c}_1 = -\mathbf{r}_2 + \mathbf{r}_3$, and cyclic permutations. The isogonal deformation tensor F^I is defined via $F^I \cdot \tau_{\mu} = \mathbf{c}_{\mu}$. We can write this in matrix form

$$F^I \begin{pmatrix} | & | \\ \tau_1 & \tau_2 \\ | & | \end{pmatrix} = \begin{pmatrix} | & | \\ \mathbf{c}_1 & \mathbf{c}_2 \\ | & | \end{pmatrix}. \quad (\text{C1})$$

Solving for F^I yields

$$F^I = \begin{pmatrix} | & | \\ \mathbf{c}_1 & \mathbf{c}_2 \\ | & | \end{pmatrix} \begin{pmatrix} | & | \\ \tau_1 & \tau_2 \\ | & | \end{pmatrix}^{-1} \quad (\text{C2a})$$

$$= \frac{1}{2\tilde{a}} \begin{pmatrix} | & | \\ \mathbf{c}_1 & \mathbf{c}_2 \\ | & | \end{pmatrix} \begin{pmatrix} -\tau_2^{\perp} & - \\ -\tau_1^{\perp} & - \end{pmatrix} \quad (\text{C2b})$$

$$= \frac{1}{2\tilde{a}} (\mathbf{c}_1 \otimes \tau_2^{\perp} - \mathbf{c}_2 \otimes \tau_1^{\perp}) \quad (\text{C2c})$$

where $2\tilde{a} = \tau_1 \wedge \tau_2$ is twice the area of the tension triangle. Now we can substitute the expressions for \mathbf{c}_{μ} in terms of \mathbf{r}_1 and use that $\tau_1 + \tau_2 + \tau_3 = 0$ to arrive at the expression Eq. (19):

$$F^I = \frac{1}{2\tilde{a}} \sum_{\mu} \mathbf{r}_{\mu} \otimes \tau_{\mu}^{\perp} = \frac{1}{2\tilde{a}} \sum_{\mu} \ell_{\mu} \tau_{\mu} \hat{\mathbf{r}}_{\mu} \otimes \hat{\mathbf{r}}_{\mu} \quad (\text{C2d})$$

From this, we recognize that F^I is always symmetric, as we expect for isogonal deformations. Moreover, in the above equation, we already recognize the form of the Batchelor formula Eq. (C1). However, the area is that of the tension triangle rather than that of the cell tessellation. Using that $\det F^I = a/\tilde{a}$, where a is the centroid triangle area $a = \frac{1}{2} \mathbf{c}_1 \wedge \mathbf{c}_2$, we find the Batchelor stress as

$$\sigma = \frac{F^I}{\det F^I} = \frac{1}{2a} \sum_{\mu} \ell_{\mu} \tau_{\mu} \hat{\mathbf{r}}_{\mu} \otimes \hat{\mathbf{r}}_{\mu}. \quad (\text{C3})$$

2. Discretization and coarse-graining of stress tensors on triangulations

In this appendix, we show how to relate discretized and continuum descriptions of stress on triangulations. As noted in Sec. 1C, we work with the “mechanical Legendre dual” of the tension network (i.e., a triangular “truss” network with force ℓ_{ij} on each link). A continuum stress $\tilde{\sigma}$ is discretized to edge values $\tilde{\sigma}_{ij}$ which can be interpreted as edge tensions. As we will now show, the scheme is physically consistent: discretizing the continuum equation $\operatorname{div} \tilde{\sigma} = 0$ reproduces the “microscopic” force-balance equations (Eq. (C5)). Via the Maxwell–Cremona correspondence, the edge stresses $\tilde{\sigma}_{ij}$ are represented geometrically as the lengths ℓ_{ij} of a cell tessellation orthogonal to the triangulation. With this machinery in hand, one can relate a continuum stress $\tilde{\sigma}$ to the local tessellation geometry. In particular, we show that the Voronoi tessellation corresponds to constant, isotropic stress $\tilde{\sigma} = \mathbb{I}$.

Following Ref. [28], a continuous stress tensor field $\tilde{\sigma}(\boldsymbol{\tau})$ can be discretized onto edges ij as

$$\tilde{\sigma}_{ij} = \int (\nabla \phi_i \cdot \tilde{\sigma} \cdot \nabla \phi_j)(\boldsymbol{\tau}) d\tau^2 \quad (\text{C4})$$

In the continuum force balance corresponds to $\operatorname{div} \tilde{\sigma} = 0$. Importantly, one obtains this discretization:

$$(\operatorname{div} \tilde{\sigma})_i = - \sum_j \tilde{\sigma}_{ij} (\boldsymbol{\tau}_j - \boldsymbol{\tau}_i) \quad (\text{C5})$$

Indeed, following Ref. [27], let us use a ‘partition of unity’: since $\boldsymbol{\tau} = \sum_j \boldsymbol{\tau}_j \phi_j(\boldsymbol{\tau})$, we can write

$$\mathbb{I} = \nabla \boldsymbol{\tau} = \nabla(\boldsymbol{\tau} - \boldsymbol{\tau}_i) = \nabla \left[\sum_j (\boldsymbol{\tau}_j - \boldsymbol{\tau}_i) \phi_j(\boldsymbol{\tau}) \right] \quad (\text{C6})$$

Using this trick, integration by parts, and the definition of $\tilde{\sigma}_{ij}$, we get:

$$\begin{aligned} (\operatorname{div} \tilde{\sigma})_i &= \int \phi_i (\nabla \cdot \tilde{\sigma}) d^2 \tau = - \int \tilde{\sigma} \cdot \nabla \phi_i d^2 \tau \\ &= - \int \nabla \boldsymbol{\tau} \cdot \tilde{\sigma} \cdot \nabla \phi_i d^2 \tau \\ &= \sum_j (\boldsymbol{\tau}_i - \boldsymbol{\tau}_j) \int \nabla \phi_j^T \cdot \tilde{\sigma} \cdot \nabla \phi_i d^2 \tau \\ &= \sum_j \tilde{\sigma}_{ij} (\boldsymbol{\tau}_i - \boldsymbol{\tau}_j) \end{aligned} \quad (\text{C7})$$

Now compare Eq.(C5) to the discrete force balance equation for the mechanical dual

$$\sum_j \frac{\ell_{ij}}{\tau_{ij}} (\boldsymbol{\tau}_j - \boldsymbol{\tau}_i) = 0 \quad (\text{C8})$$

Hence, for a balanced stress, the edge values can be interpreted geometrically,

$$\tilde{\sigma}_{ij} = \ell_{ij} / \tau_{ij} \quad (\text{C9})$$

Indeed, the primal-dual length ratio ℓ_{ij}/τ_{ij} is the flux of dual tension through edge ij . Eq. (C9) is a manifestation of the *Maxwell–Cremona* correspondence: stresses on triangular networks are equivalent to orthogonal duals (i.e., tessellations with one cell per triangulation vertex so that corresponding triangle and tessellation edges are orthogonal).

Eq. (C9) connects the discretized stress with the geometry of the dual tessellation. As we argued in the main text, all dual tessellations are parametrized by the isogonal mode θ_i . To relate the large-scale stress tensor $\tilde{\sigma}$ to θ_i , we hence need to calculate the isogonally deformed edge lengths ℓ_{ij}^I / τ_{ij} . For a kite $ijkl$ (two adjacent triangles) with inner edge ij :

$$\frac{\ell_{ij}^I}{\tau_{ij}} = \frac{|(\mathbf{r}_{ijk}^V - \mathbf{r}_{ijl}^V) + ((\nabla \theta)_{ijk} - (\nabla \theta)_{ijl})|}{\tau_{ij}} \quad (\text{C10})$$

Crucially, isogonal modes do not rotate edges, such that $\mathbf{r}_{ijk}^V - \mathbf{r}_{ijl}^V$ is parallel to $(\nabla \theta)_{ijk} - (\nabla \theta)_{ijl}$. Hence:

$$\frac{\ell_{ij}^I}{\tau_{ij}} = \frac{\ell_{ij}^V}{\tau_{ij}} + \hat{\boldsymbol{\tau}}_{ij}^\perp \cdot \frac{(\nabla \theta)_{ijk} - (\nabla \theta)_{ijl}}{\tau_{ij}}, \quad (\text{C11})$$

where $\hat{\boldsymbol{\tau}}_{ij}^\perp = \epsilon \boldsymbol{\tau}_{ij} / \tau_{ij}$ is the unit vector along $\mathbf{r}_{ijk}^V - \mathbf{r}_{ijl}^V$. The second term in Eq. (C11) computes the difference of gradients across neighboring triangles – this is a discrete 2nd derivative. Indeed, it is the Hessian of θ , rotated by $\frac{\pi}{2}$, and projected to ij (the 2nd derivative *orthogonal* to $\boldsymbol{\tau}_{ij}$). We hence find:

$$\frac{\ell_{ij}^I}{\tau_{ij}} = \frac{\ell_{ij}^V}{\tau_{ij}} + \hat{\boldsymbol{\tau}}_{ij}^T \cdot (\epsilon \cdot \operatorname{Hess}(\theta) \cdot \epsilon^T) \cdot \hat{\boldsymbol{\tau}}_{ij} \quad (\text{C12})$$

where $\operatorname{Hess}(\theta)$ is the Hessian of θ . Explicitly, one has:

$$\begin{aligned} \frac{\ell_{ij}^I}{\tau_{ij}} &= \frac{1}{2} (\cot \tilde{\gamma}_{ij}^k + \cot \tilde{\gamma}_{ij}^l) \\ &+ \frac{1}{2\tau_{ij}^2} (\theta_{jk} \cot \tilde{\gamma}_{jk}^i + \theta_{ik} \cot \tilde{\gamma}_{ik}^j \\ &+ \theta_{jl} \cot \tilde{\gamma}_{jl}^i + \theta_{il} \cot \tilde{\gamma}_{il}^j) \end{aligned} \quad (\text{C13})$$

where $\theta_{ij} = \theta_i - \theta_j$. For an equilateral triangulation, the second term is a finite-differences style second derivative: $-(\theta_k - (\theta_i + \theta_j) + \theta_l) / \tau_{ij}^2$.

An important special case is $\theta_i = 0$, i.e. the tessellation is Voronoi. Then, $\ell_{ij} = \ell_{ij}^V = \tau_{ij} (\cot \tilde{\gamma}_{ij}^k + \cot \tilde{\gamma}_{ij}^l) / 2$. We hypothesize that the corresponding large-scale stress is isotropic and uniform, $\tilde{\sigma} = \mathbb{I}$. Using Eq. (C4), one finds that the discretized “edge stresses” are

$$\mathbb{I}_{ij} = (\cot \tilde{\gamma}_{ij}^k + \cot \tilde{\gamma}_{ij}^l) / 2 = \frac{\ell_{ij}^V}{\tau_{ij}}. \quad (\text{C14})$$

Hence, the interpolation scheme confirms the result obtained for a regular lattice: for the Voronoi configuration, the stress tensor is constant and isotropic. Any balanced stress can be expressed as the double-curl of an Airy function $s \tilde{\sigma}_{ab} = \epsilon_{ac}\epsilon_{bd}\partial_{t_c}\partial_{t_d}\tilde{\psi}$. For the Voronoi case, $\tilde{\sigma}_{ab} = \delta_{ab} = (\epsilon_{ac}\partial_c)(\epsilon_{bd}\partial_d)(\frac{1}{2}|\boldsymbol{\tau}|^2)$. By Eq. (C11), the full Airy function is $\frac{|\boldsymbol{\tau}|^2}{2} + \theta(\boldsymbol{\tau})$. This completes the argument presented in Sec. IC.

We next obtain an expression for the continuum stress tensor $\tilde{\sigma}$ in terms of the discrete stresses $\tilde{\sigma}_{ij}$, inverting the discretization Eq. (C4). We place localized stress dipoles on triangulation edges:

$$\tilde{\sigma}(\boldsymbol{\tau}) = \sum_{ij} \tilde{\sigma}_{ij} \boldsymbol{\tau}_{ij} \otimes \boldsymbol{\tau}_{ij} \frac{\delta_{ij}(\boldsymbol{\tau})}{\tau_{ij}} \quad (\text{C15})$$

where $\delta_{ij}(\boldsymbol{\tau})$ is the Dirac-delta function on an edge (ij) . To obtain a smooth stress tensor, one must average the distributional tensor Eq. (C15) over an area a (triangle, cell, ...). This is the *Batchelor formula* [22]:

$$\tilde{\sigma}(\boldsymbol{\tau}) = \frac{1}{\tilde{a}} \int \tilde{\sigma}(\boldsymbol{\tau}) d^2\boldsymbol{\tau} = \frac{1}{\tilde{a}} \sum_{ij \in \tilde{a}} \ell_{ij} \boldsymbol{\tau}_{ij} \hat{\boldsymbol{\tau}}_{ij} \otimes \hat{\boldsymbol{\tau}}_{ij} \quad (\text{C16})$$

As noted in Sec. IC, the Batchelor formula implies that physical and dual stresses are inverses of one another, up to a potential multiplicative factor, $\sigma(\mathbf{r}(\boldsymbol{\tau})) \cdot \tilde{\sigma}(\boldsymbol{\tau}) \propto \mathbb{I}$. This is a consequence of the 2×2 matrix inverse formula,

$$M^{-1} = -\frac{1}{\det M} \boldsymbol{\epsilon} \cdot M^T \cdot \boldsymbol{\epsilon} \quad (\text{C17})$$

Physical and dual stress dipoles are rotated by $\frac{\pi}{2}$ with respect to one another.

The stress-dipole interpolation Eq. (C15) allows reconstructing a continuum stress tensor from edge values $\tilde{\sigma}_{ij}$. A direct calculation, using the finite-element relations Eq. (A3), shows that Eqs. (C4) and (C15) are compatible: discretizing the interpolated stress gives back the same edge values $\tilde{\sigma}_{ij}$:

$$\int \nabla \phi_i \cdot \left[\sum_{kl} \frac{\boldsymbol{\tau}_{kl} \otimes \boldsymbol{\tau}_{kl}}{t_{kl}} \delta_{kl}(\boldsymbol{\tau}) \right] \cdot \nabla \phi_j d^2\boldsymbol{\tau} = 1 \quad (\text{C18})$$

Appendix D: Pressure and conformal mode

1. Change of interface curvature by a conformal map

Here, we derive Eq. (24). Consider a line $z(t)$ with normal \mathbf{n} . The rotation of the local tangent is given by

the vorticity $\omega = \text{Im} \log f'$ of the conformal map. Moving a step dt along the transformed curve $f(z(t))$, the tangent rotates by an angle $d\phi = \omega(f(z(t+dt)) - \omega(f(z(t)) = \mathbf{n}^\perp \cdot \nabla \omega dt$. Due to the scaling factor λ , the arc length is λdt . Finally, by the Cauchy-Riemann equation Eq. (34), $\partial_a \omega = \epsilon_{ba} \partial_b \log \lambda$. Putting this together, the transformed curvature reads:

$$\kappa^C = \frac{d\phi}{d(\lambda t)} = \frac{1}{\lambda} \mathbf{n}^\perp \cdot \nabla \omega \quad (\text{D1})$$

$$= \frac{1}{\lambda} \mathbf{n} \cdot \nabla \log \lambda = \mathbf{n} \cdot \nabla \lambda^{-1} \quad (\text{D2})$$

In case the curve $z(t)$ already has curvature κ , we need to add vorticity-induced and (rescaled) initial curvature, resulting in Eq. (24).

2. Conformally deformed stress remains balanced

Note that this derivation considers only flat conformal maps. For brevity, we denote derivatives as $\partial_a h = h_{,a}$ below. To show that the conformally deformed stress Eq. (38) remains balanced, first rewrite

$$\sigma = \frac{p_0}{\lambda} R^C(\omega) \cdot \frac{F^I}{\det F^I} \cdot R^C(\omega)^T - p \mathbb{I} \quad (\text{D3a})$$

$$= \frac{1}{\lambda} \epsilon R^C(F^I)^{-1} (R^C)^T \epsilon^T - p \mathbb{I} \quad (\text{D3b})$$

The inverse isogonal deformation tensor is hence $(F^I)_{ab}^{-1} = \delta_{ab} - \partial_a \partial_b \theta^*$, where the derivatives are taken w.r.t. conformally undeformed coordinates \mathbf{r}^I . We use Θ for the Hessian matrix, $\Theta_{ab} = \theta^*_{,ab}$.

Let us first consider the case of small conformal displacement, $\lambda = 1 + \delta\lambda$, $\omega = 0 + \delta\omega$, working to linear order. We expand the Cauchy-Riemann Eq. (34) and the Young-Laplace Eq. (35):

$$\partial_a \delta\omega = -\epsilon_{ab} \partial_b \delta\lambda \quad (\text{D3c})$$

$$\partial_a p = -p_0 (F^I)_{ab}^{-1} \partial_b \delta\lambda \quad (\text{D3d})$$

To first order, the stress tensor reads:

$$\sigma_{ab} \approx p_0 (1 - \delta\lambda) [\epsilon(1 - \omega\epsilon)(1 - \Theta)(1 + \omega\epsilon)(-\epsilon)]_{ab} - p \delta_{ab} \quad (\text{D3e})$$

$$\approx p_0 \delta_{ab} + p_0 (1 - \delta\lambda) (\epsilon\Theta\epsilon)_{ab} - \omega [\epsilon, \Theta]_{ab} - (p_0 \delta\lambda + p) \delta_{ab}. \quad (\text{D3f})$$

We can now calculate the divergence of σ :

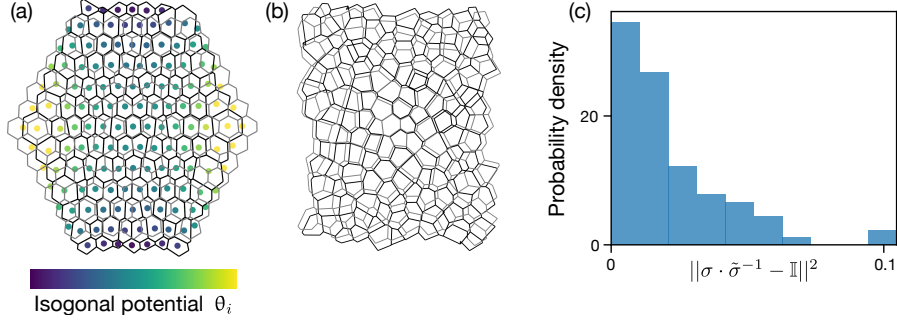


FIG. 13. (a) Parabolic isogonal mode (color code) results in pure shear. (b) Disordered cell tessellation. A disordered tension triangulation was generated via hard-disk packing [9]. Gray shows the Voronoi dual of the triangulation, deformed by the addition of an isogonal deformation into the black tessellation. The isogonal mode comprises a parabolic (shear) and a white noise component. (c) Evaluation of inverse-stress formula on disordered tessellation (b). Per-cell dual and primal stresses were calculated using the Batchelor formula Eq. (22b).

$$\frac{\lambda}{p_0}(\operatorname{div} \sigma)_b = \lambda \frac{\partial r_a^I}{\partial r_c^C} \partial_c \sigma_{ab} = R_{ca} \partial_c \sigma_{ab} \approx (\delta_{ac} - \omega \epsilon_{ac}) \partial_c \sigma_{ab} \quad (D4a)$$

$$= (\delta_{ac} - \omega \epsilon_{ac}) \{ (1 - \delta\lambda)(\epsilon \Theta_{,c} \epsilon)_{ab} - \delta\lambda_{,c} (\epsilon \Theta \epsilon)_{ab} - \omega_{,c} [\epsilon, \Theta]_{ab} - \omega [\epsilon, \Theta_{,c}]_{ab} - (p_0^{-1} p + \delta\lambda)_{,c} \}$$

$$\approx \{ (1 - \delta\lambda)(\epsilon \Theta_{,a} \epsilon)_{ab} - \omega [\epsilon, \Theta_{,a}]_{ab} - \omega \epsilon_{ac} (\epsilon \Theta_{,c} \epsilon)_{ab} \} \quad (D4b)$$

$$+ \{ \omega_{,a} [\epsilon, \Theta]_{ab} - \delta\lambda_{,a} (\epsilon \Theta \epsilon)_{ab} - (p_0^{-1} p + \delta\lambda)_{,b} \} + \mathcal{O}(\omega^2, \omega \cdot \delta\lambda). \quad (D4c)$$

In lines (b) and (c), we have grouped terms without and with gradients in $\delta\lambda$, $\delta\omega$. Expanding the commutator and using $(\epsilon \Theta_{,a})_{ab} = \partial_a \epsilon_{ac} \partial_c \partial_b \theta^* = 0$, the non-gradient terms vanish (as expected for a rigid rotation):

$$(1 - \delta\lambda)(\epsilon \Theta_{,a} \epsilon)_{ab} - \omega [\epsilon, \Theta_{,a}]_{ab} - \omega \epsilon_{ac} (\epsilon \Theta_{,c} \epsilon)_{ab} \quad (D4d)$$

$$= (1 - \delta\lambda)(\epsilon \Theta_{,a})_{ac} \epsilon_{cb} - \omega [(\epsilon \Theta_{,a})_{ac} \epsilon_{cb}] \quad (D4e)$$

$$- \theta_{,aac} \epsilon_{cb} + \epsilon_{ac} \epsilon_{ad} \theta_{,dec} \epsilon_{eb}] \quad (D4e)$$

$$= -\omega (-\theta_{,aac} \epsilon_{cb} + \theta_{,cec} \epsilon_{eb}) = 0. \quad (D4f)$$

For the gradient terms, we expand and use Eqs. (D3d):

$$\frac{\lambda}{p_0}(\operatorname{div} \sigma)_b = -\omega_{,a} [\epsilon, \Theta]_{ab} - \delta\lambda_{,a} (\epsilon \Theta \epsilon)_{ab} - (\delta\lambda + p/p_0)_{,b} \quad (D4g)$$

$$= \epsilon_{ac} \delta\lambda_c [\epsilon, \Theta]_{ab} - \delta\lambda_{,a} (\epsilon \Theta \epsilon)_{ab} - (\delta\lambda + p/p_0)_{,b} \quad (D4h)$$

$$= \delta\lambda_{,a} (\epsilon \Theta \epsilon)_{ab} + \delta\lambda_{,a} \Theta_{ab} - \delta\lambda_{,a} (\epsilon \Theta \epsilon)_{ab} - \partial_b (\delta\lambda + p/p_0) \quad (D4i)$$

$$= -(\delta_{ab} - \Theta_{ab}) \partial_a \delta\lambda - \partial_b p/p_0 \quad (D4j)$$

$$= -((F^I)_{ab}^{-1} \partial_a \delta\lambda + \partial_b p/p_0) = 0. \quad (D4k)$$

While we have carried out the calculation for small $\delta\lambda, \delta\omega$, it readily generalizes to any conformal displacement. Indeed, for constant scale-rotation, it is clear that the stress remains balanced, so one can always locally expand λ and ω as above. Note that the balance of

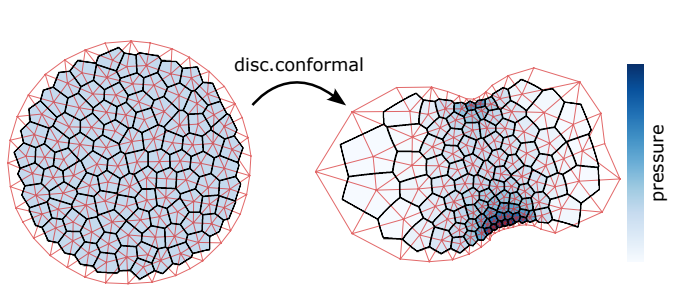


FIG. 14. Example of a non-trivial discrete conformal map from the disk to an irregular shape. Note that the map is not globally a Möbius transformation. The dual cell tilings are the corresponding MWVTs.

the stress tensor crucially relies on the Cauchy–Riemann equations. An arbitrary deformation does not lead to a balanced stress.

Appendix E: Multiplicatively weighted tessellations and discrete conformal maps

1. Vertex angles of MWVTs

Here, we show that the vertex angles in an MWVT (τ^C, λ_i) are complementary to the underlying tension triangulation with edge lengths $\tau_{ij} = |\tau_i^C - \tau_j^C|/\sqrt{\lambda_i \lambda_j}$. We find an MT that locally maps an unweighted Voronoi tes-

sellation onto a given MWVT. Consider a single tension triangle (ijk) and an MT M_{ijk} that has scale factors $|\partial_z M_{ijk}(\tau_l)| = \lambda_l$ for $l \in \{i, j, k\}$. Note that this fixes three of the six real coefficients of the MT and leaves rigid rotation and translation degrees of freedom, which can then be used to fit adjacent triangles together.

As we saw in Eq. (29), $M_{ijk}(\tau_i) = \tau_i^C$ acts as a discrete conformal map on the τ_i . Applied to the Voronoi edges, M_{ijk} yields the circular arcs of the MWVT with seed points τ_i^C and weights λ_i . This follows directly by applying Eq. (29) to the MWVT's definition. Force balance at the mapped vertex $M_{ijk}(\mathbf{r}_{ijk})$ trivially follows because MTs preserve intersection angles. As an aside, observe that under M_{ijk} , the Voronoi edges (ij) , (jk) , (ik) , extended to infinite lines, map to circles which intersect twice: Once at $M_{ijk}(\mathbf{r}_{ijk})$ and once at \mathbf{r}_{ijk}^* , the image of the point at infinity (Fig. 5). This implies that the centers of these circles must be co-linear, which was previously shown in Ref. [7, 31].

Importantly, the MTs of adjacent triangles (ijk) , (ijl) applied to the infinite extension of their shared Voronoi edge (ij) yields the same Appolonian circle, because by construction $|M'_{ijk}(\tau_i)| = |M'_{ijl}(\tau_i)| = \lambda_i$, $|M'_{ijk}(\tau_j)| = |M'_{ijl}(\tau_j)| = \lambda_j$ and $M_{ijk}(\tau_i) = M_{ijl}(\tau_i) = \tau_i^C$, $M_{ijk}(\tau_j) = M_{ijl}(\tau_j) = \tau_j^C$. However, in general $M_{ijk}(\mathbf{r}_{ijk}) \neq M_{ijl}(\mathbf{r}_{ijk})$. Put differently, the local MTs do not act continuously on individual points, but they do act continuously (even smoothly) on circular arcs [21]. This allows piecing adjacent MTs together. Hence, given a set of scale factors λ_i , the triangle-wise MTs applied to a Voronoi tessellation yield exactly the MWVT for which force balance with the original tensions and pressures $p_i = \lambda_i^{-1}$.

2. Decorated discrete conformal maps and MWPTs

A discrete conformal map of a decorated triangulation and the associated power tessellation are defined as a triangle-wise MT, with scale-factors at the vertices [21]. Fig. 15 shows an example of an MT of a decorated triangle. We define the local scale factors as the ratios of deformed and undeformed radii:

$$\lambda_i = \sqrt{\theta_i^{\text{PC}}}/\sqrt{\theta_i} \quad (\text{E1})$$

An MT leaves a certain measure of distance between circles invariant, namely the *inversive distance* $(|\tau_i - \tau_j|^2 - \theta_i - \theta_j)/\sqrt{\theta_i \theta_j}$. This implies that, under a discrete conformal map, the distance between the vertex circle centers changes as

$$\tau_{ij}^2 \mapsto (\tau_{ij}^{\text{PC}})^2 = |\tau_i^{\text{PC}} - \tau_j^{\text{PC}}|^2 \quad (\text{E2a})$$

$$= \lambda_i \lambda_j \tau_{ij}^2 + (\lambda_i - \lambda_j)(\lambda_i \theta_i - \lambda_j \theta_j). \quad (\text{E2b})$$

This relation generalizes Eq. (28) and thus defines the discrete conformal mapping of a decorated triangulation. Comparing Eq. (28) with Eq. (7) from Ref. [8] shows that

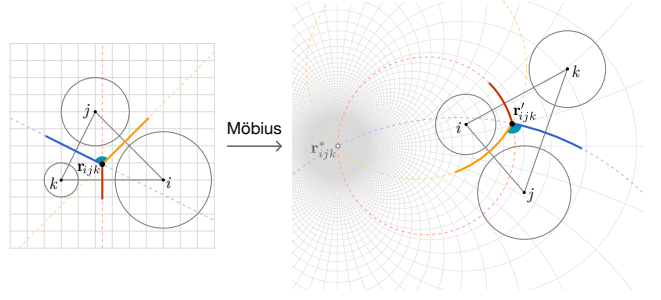


FIG. 15. Möbius transformation of a single triangle decorated by power circles with the corresponding vertex and edges of the power diagram. Note that one maps the power circles, not the power circle centers. The Power Diagram is mapped to a Multiplicatively Weighted Power tessellation (MWPT), where the scale factors of the Möbius transformation give the weights.

MWPTs satisfy the Young–Laplace law. (To compare with Ref. [8], the notational equivalents are $\tau_i \mapsto \mathbf{q}_\alpha$, $\lambda_i \mapsto p_\alpha^{-1}$, $\kappa_{ij} \mapsto R_{\alpha\beta}^{-1}$, and $\theta_i \mapsto z_\alpha^2$).

Appendix F: Continuum limit of isogonal modes non-flat triangulations

In App. A 2, we argue that in the continuum limit $\Delta^I h = (\det F^I)^{-1} \nabla_{\tau} \cdot (\det F^I (F^I)^{-1} \nabla_{\tau} h)$, where F^I is the isogonal deformation tensor. Combined with the continuum Young–Laplace law $\nabla_{\tau} p = F^I \nabla_{\tau} \lambda^{-1}$ [Eq. (35)], $\Delta^I \log p = K$ implies the following continuum equation for the conformal factor

$$(\det F^I)^{-1} \nabla_{\tau} \cdot (\det F^I (F^I)^{-2} \nabla_{\tau} \log \lambda) \quad (\text{F1})$$

$$= \Delta_{g^I} \log \lambda = -\lambda^{-2} K \quad (\text{F2})$$

Here, we identified the Laplace–Beltrami operator $\Delta_{g^I} h = \sqrt{\det g^I}^{-1} \nabla_{\tau} \cdot [\sqrt{\det g^I} (g^I)^{-1} \cdot \nabla_{\tau} h]$ of the isogonal metric $g^I = F^I \cdot g \cdot (F^I)^T$.

We therefore arrive at the following interpretation. An isogonal deformation F^I stretches and compresses cells, deforming the metric g of the tension manifold to that of the (non-planar) isogonal tessellation, $g^I = F^I \cdot g \cdot (F^I)^T$ (see Fig. 16). The isogonal mode acts in the local tangent plane of the non-planar triangulation without changing the curvature K , and can therefore be absorbed into a coordinate change. Hence, the conformal factor λ is independent of the isogonal mode, while the pressure p depends on the isogonal mode via Eq. (35).

Explicitly, the isogonal displacement in the presence of conformal deformation is given by

$$\begin{aligned} r_a \mapsto r_a^I &= r_a + (g^{-1}(\tau))_{ab} \partial_b \theta \\ &= r_a + \lambda^2 \partial_a \theta \end{aligned} \quad (\text{F3})$$

The Riemannian metric reflects that the isogonal displacement takes place on the tension manifold. This

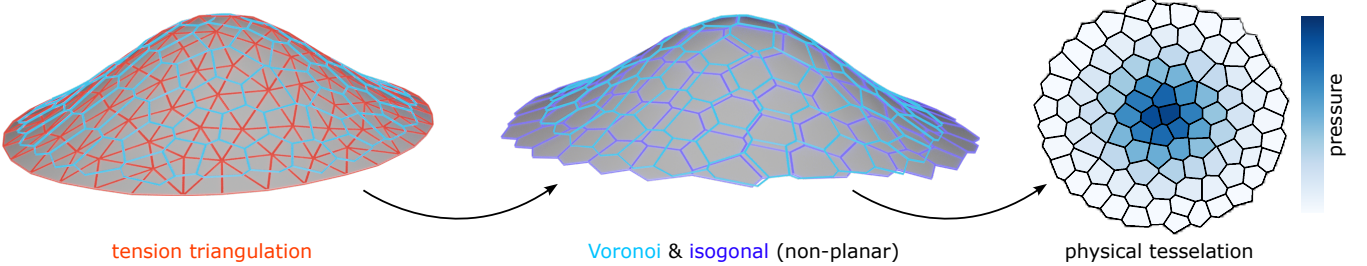


FIG. 16. (Left) Non-planar tension triangulation (red) and Voronoi reference state (light blue). (Middle) The triangulation is mapped to a curved cell tessellation (blue) via the isogonal mode, which displaces vertices in the local tangent plane. (Right) The non-planar tessellation is conformally mapped to the physical, flat tessellation, creating pressure differentials. Flat tessellation is an MWPT obtained by numerical optimization of 2d seeds and conformal factors (τ_i^C, λ_i) to fulfill Eq. (E2) for the given tension triangulation and isogonal mode.

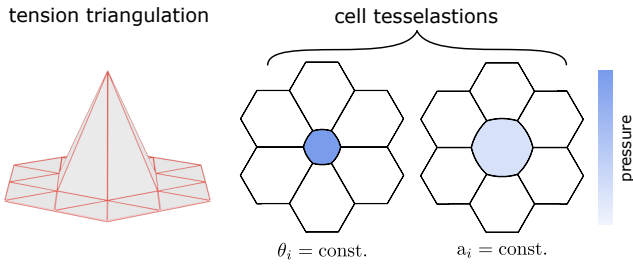


FIG. 17. Interplay of pressure and isogonal mode. A non-planar tension triangulation (left) discrete-conformally is mapped to a planar cell tessellation (center, right). The resulting pressure differential depends on the isogonal mode: compared to the Voronoi case (center), isogonally inflating the central cell so all cell areas are equal (right) lowers the pressure gradient. With longer cell-cell interfaces, a smaller interface curvature suffices to compensate for the angle deficit.

matches the form for the isogonal displacement for a non-flat tension metric identified in the companion paper. For a flat conformal deformation $r \mapsto f(r_1 + ir_2)$, Eq. (F3) can be derived by means of a Taylor expansion:

$$\begin{aligned} f(z + \nabla\theta) &\approx f(z) + (\partial_z f)\nabla\theta \\ &= f(z) + \lambda^2 \nabla_{f(z)}\theta \end{aligned} \quad (\text{F4})$$

This makes it clear that the continuum interpretation is valid when the isogonal displacement is small compared to the scale $1/\nabla\lambda \sim 1/\sqrt{K}$ of the tension manifold curvature.

Appendix G: Triangle shape via local tension configuration parameters

The local configuration of tension is encoded in the shape of tension triangles. In Refs. [9, 17], we introduced local tension configuration (LTC) parameters based on the singular value decomposition of the linear map T from an equilateral reference triangle to the target triangle. On a triangle, T can be defined by linear interpolation

Given 2D vertices $\zeta_{1,2,3}$ of the equilateral reference triangle and $\tau_{1,2,3}$ of the target tension triangle, we can define $T(\zeta) = \sum_{i=1,2,3} \phi_i(\zeta) \tau_i$ using the barycentric interpolation of App. A. T is therefore a linear map.

The single value decomposition of a 2×2 matrix $T = R(\phi_T) \cdot \Sigma \cdot R(\psi)^T$ specifies two angles and a diagonal matrix of stretch factors

$$\Sigma := \sqrt{S} \operatorname{diag}(m, 1/m), \quad m = \left(\frac{1 + |\mu_T|}{1 - |\mu_T|} \right)^{\frac{1}{4}} \quad (\text{G1})$$

The scale factor S is proportional to the area of the triangle (i.e. the local scale of tension). In the following, we will focus on scale-invariant features of the triangle shape, characterized by the tuple $(\mu_T, \psi) \in \mathbb{C} \otimes \mathbb{R}$, which we refer to as LTC parameters. The angle ψ accounts for the orientation of shear relative to the orientation of the equilateral reference triangle. It therefore tunes the triangle's shape between acute and obtuse. The reference triangle edges after rotation by ψ read

$$\hat{\Psi}_i := \begin{pmatrix} \cos(\psi + \frac{2(\alpha-1)\pi}{3}) \\ \sin(\psi + \frac{2(\alpha-1)\pi}{3}) \end{pmatrix} \quad (\text{G2})$$

Due to invariance of shape under permutation of the edge labels $i = \{1, 2, 3\}$, ψ can be restricted to the fundamental domain $[-\pi/6, \pi/6]$. Applying the stretch and second rotation yields the triangle edge vectors

$$\tau_i = R(\phi_T) \cdot \Sigma_T \cdot \hat{\Psi}_i. \quad (\text{G3})$$

The angle, which we refer to as ‘‘LTC phase’’ ϕ_T , therefore, determines the orientation of the triangle's principal axes in real space. This ‘‘extrinsic’’ shape information is contained in the tensor

$$\mathbb{T} := \sum_i \tau_i \otimes \tau_i = R(\phi_T) \cdot \Sigma_T^2 \cdot R(\phi_T)^T, \quad (\text{G4})$$

which is independent of the LTC phase ψ . The Beltrami coefficient of the quadratic form \mathbb{T} is given by $\mu_T = |\mu_T| e^{2i\phi_T}$ with $|\mu_T| = (2 \operatorname{Tr}[\tilde{\mathbb{T}}^2])^{1/2} / \operatorname{Tr}[\mathbb{T}]$, where $\tilde{\mathbb{T}}$ denotes the traceless part of \mathbb{T} . It compactly encodes information about the magnitude and orientation of tension anisotropy.

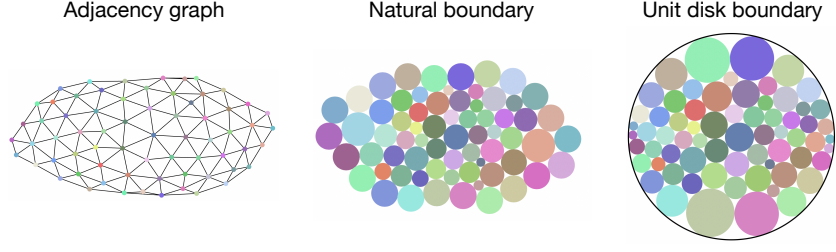


FIG. 18. Boundary conditions for Thurston circle packs.

Appendix H: T1 threshold

We calculate the T1 threshold for a kite formed from two identical tension triangles. To parametrize the tension triangle shape, we use the local tension configuration (LTC) parameters; see App. G.

To find the T1 threshold as a function of the isogonal deformation (i.e., macroscopic stress) and LTC parameters, we need to find the edge lengths ℓ_α . From Eq. (19), one sees that F is linear in the ℓ_α such that finding the edge lengths is achieved by solving a linear set of equations. Since the overall scale factor $\det F^I$ is irrelevant, we can arbitrarily fix it with the simple linear constraint

$$\ell_1 + \ell_2 + \ell_3 = 1 \quad (H1)$$

and simultaneously solve for s such that this constraint is fulfilled. Note that because the overall scale of ℓ_i is irrelevant, the conformal mode F^C does not play any role in the T1-threshold.

The linear system of equations to be solved for ℓ_α and scale factor s_0 then reads

$$\sum_\alpha \frac{\ell_\alpha}{t_\alpha} \boldsymbol{\tau}_\alpha^\perp \otimes \boldsymbol{\tau}_\alpha^\perp - s_0 F^I = 0, \quad (H2)$$

$$\sum_\alpha \ell_\alpha = 1. \quad (H3)$$

Using the notation, $\boldsymbol{\tau}_\alpha^\perp/t_\alpha = \hat{\mathbf{r}}_\alpha = (\hat{x}_\alpha, \hat{y}_\alpha)$, the solution to these equations reads

$$\ell_1 \propto (F_{xx}^I \hat{y}_2^2 - F_{yy}^I \hat{x}_2^2) \hat{x}_3 \hat{y}_3 + F_{xy}^I \hat{x}_2^2 \hat{y}_3^2 - (2 \leftrightarrow 3),$$

and corresponding cyclic permutations for $\ell_{2,3}$. We suppress the prefactor since we are ultimately interested in the T1 threshold $\ell_\alpha = 0$. Through some straightforward algebra, one finds that Eq. (H4) can be cast in the manifestly invariant form

$$\ell_1 \propto \text{Tr} \{ F^I \cdot [(\hat{\mathbf{r}}_2 \wedge \hat{\mathbf{r}}_3)(\hat{\mathbf{r}}_2^\perp \otimes \hat{\mathbf{r}}_3^\perp) - (\hat{\mathbf{r}}_3 \wedge \hat{\mathbf{r}}_2)(\hat{\mathbf{r}}_3^\perp \otimes \hat{\mathbf{r}}_2^\perp)] \}. \quad (H4)$$

or equivalently

$$\ell_1 \propto \text{Tr} \{ F^I \cdot [(\boldsymbol{\tau}_2 \wedge \boldsymbol{\tau}_3)(\boldsymbol{\tau}_2 \otimes \boldsymbol{\tau}_3) - (\boldsymbol{\tau}_3 \wedge \boldsymbol{\tau}_2)(\boldsymbol{\tau}_3 \otimes \boldsymbol{\tau}_2)] \}. \quad (H5)$$

Using $\boldsymbol{\tau}_1 + \boldsymbol{\tau}_2 + \boldsymbol{\tau}_3 = 0$, we can further simplify this to

$$\ell_1 \propto \text{Tr} \left\{ F^I \cdot \left[\sum_\alpha \boldsymbol{\tau}_\alpha \otimes \boldsymbol{\tau}_\alpha - 2\boldsymbol{\tau}_1 \otimes \boldsymbol{\tau}_1 \right] \right\} \quad (H6)$$

By substituting the expression for $\boldsymbol{\tau}_\alpha$ in terms of the LTC parameters, Eq. (G3), we obtain an explicit expression in terms of F^I, μ_T, ψ :

$$\ell_\alpha(F^I, \mu_T, \psi) \propto \text{Tr} \left\{ \Sigma_T \cdot R(\phi_T) \cdot F^I \cdot R(\phi_T)^T \cdot \Sigma_T \cdot \left[\hat{\Psi}_\alpha \otimes \hat{\Psi}_\alpha - \frac{3}{4} \mathbb{I} \right] \right\}. \quad (H7)$$

The proportionality factor is the same for all three ℓ_α .

Let us parametrize the isogonal deformation tensor as

$$F^I = s_1 \hat{\phi} \otimes \hat{\phi} + s_2 \hat{\phi}^\perp \otimes \hat{\phi}^\perp, \quad (H8)$$

where $\hat{\phi} = (\cos \phi, \sin \phi)^T$ and we use the convention $s_1 > s_2$. (This can equivalently be written as an SVD $F^I = R(\phi_I) \cdot \Sigma_I \cdot R(\phi_T)^T$ with $\Sigma_I = \text{diag}(s_1, s_2)$.) For the T1 threshold, the scale $s_1 s_2$ is irrelevant – only the orientation and magnitude of anisotropy of deformation matter. This information is captured by the Beltrami coefficient $\mu_I = |\mu_I| e^{2i\phi_I}$ with $|\mu_I| = (s_1 - s_2)/(s_1 + s_2)$. For explicit calculations using F^I in the following, we parametrize $s_1 = 1 + |\mu_I|$, $s_2 = 1 - |\mu_I|$.

A T1 happens when $\ell_\alpha(\mu_T, \mu_I, \psi) = 0$ for one of the edges α , implicitly defining a hypersurface \mathcal{C}_{T1} in the configuration space (μ_T, μ_I, ψ) which bounds the admissible configurations. Due to rotational symmetry, only the relative orientation $\phi_{T1} := \phi_I - \phi$ of shear deformation F^I and tension anisotropy ϕ_T is relevant.

Some slices of this \mathcal{C}_{T1} in the polar $(|\mu_I|, \phi_{T1})$ plane are shown in Fig. 19 for various values of $|\mu_T|$ and ψ . Parameterizing \mathcal{C}_{T1} as a graph $|\mu_I^{T1}|$ over $(|\mu_T|, \phi_{T1}, \psi)$ defines a yield strain – and hence yield stress. In fact, such a parametrization is always possible, because $\ell_\alpha = 0$ is a linear equation in $|\mu_I|$, with the explicit solution

$$|\mu_I^{T1}|(|\mu_T|, \phi_{TI}, \psi) := \frac{(\phi \cdot \Sigma_T \cdot \Psi)^2 + (\phi^\perp \cdot \Sigma_T \cdot \Psi)^2 + \frac{3}{2} \det \Sigma_T}{(\phi \cdot \Sigma_T \cdot \Psi)^2 - (\phi^\perp \cdot \Sigma_T \cdot \Psi)^2 + \frac{3}{2} |\mu_T| \cos(2\phi_{TI}) \det \Sigma_T} \quad (H9)$$

Note however that for $|\mu_T| > 1/2$, μ_I^{T1} is not always an upper threshold on μ_I . For example, in Fig. 19(d), the blue line bounds the admissible configurations from below in $|\mu_I|$. In this regime

For isotropic tension ($|\mu_T| = 0$), Eq. (H7) yields the simple expression

$$|\mu_I^{T1}|(|\mu_T| = 0, \phi_{TI}, \psi) = [2 \cos 2(-\frac{\pi}{6} + (\frac{\pi}{6} + \phi_{TI} - \psi \bmod \frac{\pi}{3}))]^{-1}. \quad (H10)$$

The corresponding graph in the polar $(|\mu_I|, \phi_{TI})$ plane is shown in Fig. 11(b). This case corresponds to an ordinary fluid foam where all surface tensions are identical. Passive T1s are driven by external (boundary) forces acting on the tissue, which drive $|\mu_I|$ toward $|\mu_I^{T1}|$. Through controlling tensions, cells can manipulate $|\mu_T|$ and thus drive *active* T1s. In particular, for $|\mu_T| = 1/2, \psi = 0$, the yield strain in the sector $|\phi_{TI}| < \pi/4$ vanishes; Fig. 20(b). This is therefore the critical tension anisotropy for which active T1s happen in the absence of isogonal deformation, i.e. in the macroscopically stress-free state. Active

T1s happen most readily for $\psi = 0$

In a disordered tissue, we will find tension triangles with all shape phases ψ . Thus, given μ_I, μ_T , we can define the minimal edge length that occurs across all ψ

$$\ell_{\min}(|\mu_I|, |\mu_T|, \phi_{TI}) := \min_{\alpha \in \{1, 2, 3\}} \min_{\psi \in [0, \pi/6]} \ell_\alpha(|\mu_I|, |\mu_T|, \phi_{TI}, \psi) \quad (H11)$$

From this, we can define the “marginal” T1 threshold as the locus $\ell_{\min}(|\mu_I|, |\mu_T|, \phi_{TI}) = 0$. This locus is rendered in Fig. 20(a) in the $(|\mu_I|, |\mu_T|)$ -plane for various values of ϕ_{TI} . It is immediately apparent that the T1 threshold is symmetric under the exchange of $|\mu_I|$ and $|\mu_T|$. In other words, the anisotropy magnitudes in tension space and real space play equivalent roles in driving T1s, i.e. there is a correspondence (or duality) between active and passive T1s. Fig. 20(b) shows T1 threshold contours in the $(|\mu_I|, \phi_{TI})$ -polar plot for different values of $|\mu_T|$. Note that a plot with the roles of μ_I and μ_T reversed would look identical due to the symmetry that is apparent in Fig. 20(a).

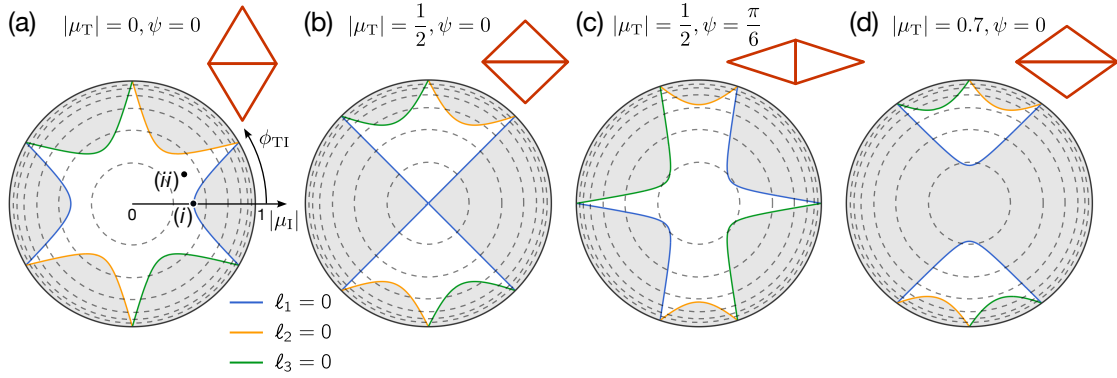


FIG. 19. (a) T1 threshold for isotropic tension $|\mu_T| = 0$ (same as panel (b) in Fig. 11). (b) Critical case $|\mu_T| = 1/2, \psi = 0$, where the Voronoi edge vanishes $\ell_1^V = 0$, i.e. a T1 takes place in the stress-free reference configuration ($|\mu_I| = 0$). This is the prototypical case of an active T1. (c) For the same tension anisotropy $|\mu_T| = 1/2$ but a “cable-like” tension configuration $\psi = \pi/6$, the T1 threshold remains at finite μ . (d) For higher tension anisotropy, active T1s happen even when the isogonal deformation is oriented opposite to the axis of tension anisotropy.

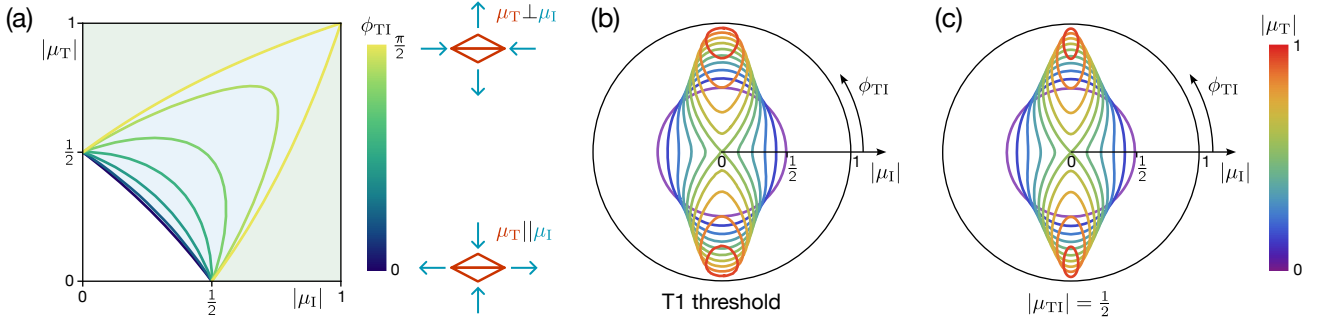


FIG. 20. (a) Marginalized T1 threshold as a function of the tension and isogonal Beltrami coefficients, μ_T and μ_I , shown in the plane of their magnitudes. The threshold depends on the relative phase of the two Beltrami coefficients, $2\phi_{TI} = \arg \mu_T - \arg \mu_I$, which measures the angle between the principal axis of tension anisotropy and the principal axis of isogonal strain. The shaded area indicates the region where at least one of the ℓ_i is negative for some value of ψ , indicating that a T1 must have happened. Note the symmetry under exchange of μ_T and μ_I . (b) Marginalized T1 thresholds as a polar plot ($|\mu_I|, \phi_{TI}$) for a range of $|\mu_T|$. Exchanging $\mu_I \leftrightarrow \mu_T$ yields the same plot. (c) Contours along which the “Beltrami sum” of μ_T and μ_I , has magnitude $1/2$. This provides a good approximation for the true marginalized T1 threshold shown in (b).